Geochimica et Cosmochimica Acta 370 (2024) 173–187

Contents lists available at ScienceDirect

Geochimica et Cosmochimica Acta

journal homepage: www.elsevier.com/locate/gca

Transformation of vivianite in intertidal sediments with contrasting sulfide conditions

L. Joëlle Kubeneck [a,*], Luiza Notini [a], Katherine A. Rothwell [a,1], Giulia Fantappiè [a], Thomas Huthwelker [b], Laurel K. ThomasArrigo [a,c], Ruben Kretzschmar [a]

[a] Soil Chemistry Group, Institute of Biogeochemistry and Pollutant Dynamics, Department of Environmental Systems Science, ETH Zürich, Universitätstrasse 16, CHN, CH-8092, Zürich, Switzerland
[b] Paul Scherrer Institut, 5232 Villigen, Switzerland
[c] Environmental Chemistry Group, Institute of Chemistry, University of Neuchâtel, Avenue de Bellevaux 51, Neuchâtel, Switzerland

ARTICLE INFO

Associate editor: Mariette Wolthers

ABSTRACT

Vivianite, a ferrous phosphate mineral, can be a significant phosphorus (P) burial phase in non-sulfidic, reducing coastal sediments. Expected sea level rise may increase sulfide production in currently non-sulfidic sediments containing vivianite, leading to conditions under which vivianite is thermodynamically unstable. Here, we compared the mineral transformation processes of two different vivianites: unsubstituted vivianite and a vivianite substituted with Mn and Mg (Mn/Mg/Fe = 0.30/0.14/0.56), two cations that frequently substitute for Fe in the crystal structure of vivianite. Further, we investigated the potential role of calcium carbonate as a sorption site for phosphate, which is released during vivianite dissolution. The vivianites were mixed with sea sand (quartz) and with or without calcium carbonate. The mixes were filled in mesh bags and installed at 15 to 20 cm sediment depth at two adjacent field plots with contrasting dissolved sulfide concentrations in an intertidal flat in the Wadden Sea. The low sulfide plot had sulfide concentrations ≤50 μM, while concentrations at the high sulfide plot ranged from 0.6 to 6.7 mM. Porewater chemistry was regularly monitored during the field experiment. After 56 days of field incubation, the reacted solid phase was assessed by acid digestion for total elemental composition and Fe, P, and S speciation by X-ray absorption spectroscopy. Both vivianites with and without calcium carbonate and at both field plots dissolved partially, resulting in a net loss of Fe, Mn, Mg, and P from the mesh bags (elemental losses ranged from ~ 10 to 35%), while solid-phase S accumulated, particularly at the high sulfide plot. Green rust minerals were the major transformation product at the low sulfide plot to which some released phosphate could likely readsorb. Mackinawite formation, which dominated at the high sulfide plot, is less efficient at adsorbing P and thus resulted in an enhanced P loss from the mesh bags. On average, there was ~ 27% P loss at the high sulfide plot, compared to ~ 20% at the low sulfide plot. Mn-Mg-substituted vivianite dissolved more at both field plots, likely due to changes in mineral reactivity due to isomorphic substitution. The presence of calcium carbonate slightly lowered P loss, suggesting that its presence may positively impact P retention during vivianite transformation. Overall, P availability was enhanced under euxinic conditions, indicating that vivianite-containing sediments may become sources of bioavailable P under changing environmental conditions.

1. Introduction

Oversupply of phosphorus (P) in the coastal ocean is often identified as a substantial driver for coastal eutrophication (Conley et al., 2009). Coastal sediments play an important role as nutrient filters by retaining and permanently removing nutrients such as P via burial (Froelich, 1988; Bouwman et al., 2013; Asmala et al., 2017). Thus, the efficiency of retaining and burying P in coastal sediments plays an essential role in maintaining overall water quality. In P and iron (Fe)-rich, non-sulfidic, reducing sediments, the ferrous phosphate mineral vivianite ($Fe_3(PO_4)_2 \cdot 8H_2O$) can be an important P burial phase (Egger et al., 2015; Dijkstra et al., 2018; Kubeneck et al., 2021). For instance, Eg-

* Corresponding author.
E-mail address: luisa.kubeneck@usys.ethz.ch (L.J. Kubeneck).
[1] Now at School of Earth Sciences, University of Bristol, Wills Memorial Building, Bristol BS8 1RJ, UK.

https://doi.org/10.1016/j.gca.2024.01.020
Received 10 October 2023; Accepted 20 January 2024
Available online 26 January 2024

ger et al. (2015) calculated that vivianite accounts for 40-50% of total P burial below the sulfate-methane transition zone (SMTZ) in Bothnian Sea sediments.

The P bound in the crystal lattice of vivianite is considered to be unavailable for organisms under non-sulfidic, reducing conditions due to the low solubility of vivianite at circumneutral pH (e.g., Heinrich et al., 2021; Brady et al., 2022). However, vivianite is thermodynamically unstable in the presence of hydrogen sulfide (denoted here as HS^- as it is the dominant species at seawater pH, Nriagu, 1972). Due to expected sea level rises, changes in bottom water salinity may enhance sulfide formation via sulfate reduction in currently non-sulfidic coastal sediments containing vivianite (Lenstra et al., 2018; Kubeneck et al., 2021). The switch from ferruginous to euxinic conditions could result in vivianite dissolution and ultimately an increase in phosphate bioavailability (Duverger et al., 2020; Bronner et al., 2023). Vivianite sulfidation could fuel future coastal eutrophication via enhanced benthic efflux of phosphate, as secondary minerals such as mackinawite are not efficient sorption phases for phosphate (Krom and Berner, 1980, 1981).

Despite the importance of understanding the destabilization of vivianite as a P burial sink for nutrient cycling, as well as potential future nutrient fluxes, vivianite transformation processes under sulfidic conditions in-situ remain unclear. However, vivianite found in some environmental samples exhibited post-depositional changes (pitting and/or dissolution of crystals) due to the presence of HS^- (Murphy et al., 2001; O'Connell et al., 2015; Dijkstra et al., 2018) and subsequently vivianite dissolution was considered as a potential cause for increasing benthic P fluxes (Murphy et al., 2001). Until now, the dissolution of vivianite upon exposure to HS^- has only been studied in laboratory slurry systems, which showed the complete dissolution of vivianite in the presence of HS^- within 100 h (Dijkstra et al., 2018; Wilfert et al., 2020). However, in natural sediments, vivianite is part of a complex sediment matrix compromising other minerals and organic matter, which likely leads to diffusion limitations and higher solid-to-solution ratios compared to model systems. Consequently, vivianite dissolution dynamics observed in model systems might not be transferable to natural systems, and questions remain about which secondary minerals may form upon vivianite transformation. As seen in model studies, we hypothesize that in a sulfidic environment, dissolution-precipitation processes likely dominate the transformation of vivianite and result in the formation of Fe-sulfide minerals, including mackinawite, greigite, and pyrite (Rickard, 1969; Berner, 1981), and FeS_x, which is defined as a metastable Fe-sulfide mineral with $x \geq 1$ (Wan et al., 2017; Thiel et al., 2019). The extent of the reaction will likely depend on the dissolved HS^- concentration. While Fe-sulfide minerals can retain the released Fe upon vivianite dissolution, they do not co-precipitate with or adsorb P (Krom and Berner, 1980, 1981). Subsequently, phosphate can either accumulate in the porewater or readsorb to other particles upon vivianite dissolution. Besides Fe-minerals, P adsorbed or co-precipitated with calcium (Ca)-minerals such calcium carbonate ($CaCO_3$), amorphous calcium-phosphates and carbonate fluorapatite can be important P burial and retention phases (Kraal et al., 2017). The transfer from one P reservoir to another, such as from P associated with Fe minerals to P associated with Ca minerals during early diagenesis in natural sediments, is known as sink-switching and plays an important role in retaining P in sediments (Ruttenberg and Berner, 1993). Thus, we hypothesize that the presence of $CaCO_3$ could lead to the (partial) retention of the released phosphate during vivianite dissolution by sorption to $CaCO_3$ and/or amorphous calcium-phosphate formation, which over long time periods might transform to carbonate fluorapatite (Gunnars et al., 2004).

Authigenic vivianite in the environment frequently contains other divalent cations, such as manganese (Mn) and magnesium (Mg), which substitute for Fe in the crystal structure (Egger et al., 2015; Dijkstra et al., 2018; Kubeneck et al., 2023). The crystal structure of vivianite has two unique Fe atom positions. One-third of the Fe atoms are present in isolated octahedral positions. The other Fe atoms are located in edge-sharing, double octahedral positions with a short interatomic Fe-Fe distance, allowing intervalence electron sharing (Mori and Ito, 1950). Isomorphic substitution of Fe by Mn or Mg occurs preferentially in the double octahedral positions (Kubeneck et al., 2023), which may thus have implications for the redox stability of vivianite. Additionally, substituting Fe by Mn and Mg results in changes in crystal structure and morphology by, for instance, increasing crystal roughness and decreasing crystallite size (Kubeneck et al., 2023), which may potentially impact the mineral's reactivity. Isomorphic substitution of Fe by other cations in various ferric and ferrous minerals has been linked to changes in solubility (Alvarez et al., 2006; Liu et al., 2018), and rates of proton-promoted, sulfidation and reductive dissolution rates (Torrent et al., 1987; Poulton et al., 2004; Ekstrom et al., 2010). For vivianite, it remains unknown how the substitution of Fe by Mn, Mg, or other divalent cations affects in-situ sulfidation and, thus, its stability as a P burial sink.

To investigate conditions leading to vivianite as a P source in sulfidic sediments, we incubated unsubstituted vivianite (Viv) and Mn-Mg-substituted vivianite (Viv_sub) mixed with or without calcium carbonate ($CaCO_3$) and with quartz sand, imitating a natural sediment matrix, at two field plots with contrasting aqueous HS^- concentrations in an intertidal flat in the Wadden Sea (Northern Germany) for 56 days. The comparison between Viv and Viv_sub provided information about how cation substitution influences mineral reactivity and mineral transformation products. In addition, the presence or absence of $CaCO_3$ in the mineral-sand mixes provided insights into how $CaCO_3$ alters the retention of the released phosphate upon vivianite dissolution. The incubated mineral-sand mixes were analyzed for their total elemental composition and speciation of Fe, P, and sulfur (S) by X-ray absorption spectroscopy (XAS) at the end of the field experiment. Our results provide new insights into the transformation of vivianite which will help to better predict and manage future P fluxes in coastal environments prone to eutrophication.

2. Materials and methods

2.1. Preparation of materials for the field experiment

2.1.1. Vivianite synthesis

The synthesis of the unsubstituted and substituted vivianite was described in Kubeneck et al. (2023). Briefly, for the synthesis of the minerals, all solutions were prepared using analytical grade chemicals with de-oxygenated and CO_2-free ultra-pure water (UPW, Milli-Q, Millipore, >18.2 MΩ ·cm). All glassware used for vivianite synthesis was acid-washed (10% hydrochloric acid (HCl), v/v) for 24 h and then rinsed thoroughly with UPW before use. Both vivianites were synthesized in an anoxic chamber (MBraun, UNIlab Plus, N_2 atmosphere, <1 ppm v/v O_2) at room temperature by precipitation. For the unsubstituted vivianite (Viv), 250 mL of 0.1 M $FeSO_4 \cdot 7H_2O$ stock solution was added to 650 mL UPW. Under continuous stirring (300 rpm), 150 mL of 391 mM Na_2HPO_4 stock solution was added. The pH was 7.0 ± 0.1 upon solution mixing and remained stable thereafter.

To synthesize the Mn-Mg-substituted vivianite (Viv_sub; final composition Mn/Mg/Fe = 0.30/0.14/0.56) at 9 psu, 250 mL of 0.1 M $FeSO_4 \cdot 7H_2O$, 100 mL of 137 mM $MnCl_2 \cdot 4H_2O$ and 262 mL of artificial seawater (35 psu, prepared after Kester et al., 1967) were added to 238 mL of UPW. Under continuous stirring (300 rpm), 150 mL of 391 mM Na_2HPO_4 stock solution was added. The Fe^{2+}, Mn^{2+} and Mg^{2+} concentrations in the precipitation solution were 25.0 mM, 13.7, and 13.7 mM, respectively. Mn-Mg-substituted vivianite formation led to slightly acidic pH conditions. The pH was readjusted to 7.0 ± 0.1 within the first 5 minutes by the addition of 2 M NaOH and thereafter, pH remained stable.

A white-grayish precipitate appeared immediately for both vivianite syntheses and the suspensions were continuously stirred at 300 rpm for

Table 1
Overview of the initial mesh bags' content for each treatment. Details on the characterization of the sea sand and $CaCO_3$ can be found in Section S2.1.

Treatment	Abbreviation	Sea sand [mg]	Viv [mg]	Viv_sub [mg]	$CaCO_3$ [mg]
Unsubstituted vivianite	*Viv*	700	280		
Unsubstituted vivianite with $CaCO_3$	*Viv+CC*	490	280		210
Mn-Mg-substituted vivianite	*Viv_sub*	700		280	
Mn-Mg-substituted vivianite with $CaCO_3$	*Viv_sub+CC*	490		280	210

Table 2
Elemental content in mesh bags prior to the field experiment calculated from the composition of initial vivianites and calcite.

Treatment	Ca [mmol/g]	Fe [mmol/g]	Mg [mmol/g]	Mn [mmol/g]	P [mmol/g]
Viv		1.79			1.08
Viv+CC	2.10	1.79			1.08
Viv_sub		1.04	0.27	0.56	1.18
Viv_sub+CC	2.10	1.04	0.27	0.56	1.18

24 h. Both synthesis solutions were supersaturated with respect to vivianite (saturation index ~ 13). The vivianite suspensions were filtered (0.45 μm, nylon) after 24 h reaction time. The recovered vivianites (4 to 6 g) were washed with 1 L UPW and dried, homogenized with agate mortar and pestle, and stored under dark and anoxic conditions. The elemental composition and mineralogy of both vivianites was characterized by acid dissolution followed by inductively coupled plasma optical emission spectrometry (ICP-OES, Agilent 5100) analysis, X-ray diffraction (XRD), ^{57}Fe-Mössbauer spectroscopy, electron microscopy, and Fe K-edge XAS (see Kubeneck et al., 2023, for detailed information).

2.1.2. Preparation of in-situ samplers

For the field experiment, four different treatments of mineral-sand mixes were prepared (Viv, Viv+calcium carbonate (CC), Viv_sub, and Viv_sub+CC). The composition and elemental content of the four different treatments are presented in Tables 1 and 2. The minerals (Viv and Viv_sub, respectively) were mixed with sea sand (Sigma Aldrich, extra pure, 0.1-0.315 mm grain size) to simulate a more natural sediment matrix. The sea sand mainly consisted of quartz (see Section S2.1 for further information). Prior to use, the sand was acid-washed (10% HCl v/v) for 24 h and then rinsed thoroughly with UPW to remove trace contamination. The sand was dried under ambient conditions at 40 °C in an oven. The mineral-sand mixes (1 g, Table 1) were filled into polyethylene terephthalate (PETE) mesh bags (1.5 cm x 5 cm, 51 μm pore size, SEFAR, Switzerland, Fig. S6A) inside an anoxic chamber. To minimize solid phase material loss through the mesh, mesh bags consisted of three mesh layers. The mesh bags were heat sealed, and the filled mesh bags were inserted into in-house designed 3D-printed sample holders (Clear Photopolymer Resin, Formlabs) with an opening of 5 cm matching the mesh bag dimensions (Fig. S6B). A threaded, labeled nylon rod was screwed onto the sample holder to allow easy insertion of the sample holder in the sediments. The insertion depth was marked on the nylon rod to ensure that the opening window of the sample holder was buried at a depth of 15 to 20 cm. The prepared sample holders, including attached nylon rods, were double-sealed in air-tight Al-bags for O_2-free transportation to the field.

2.2. Field experiment

2.2.1. Sample installation

Samples were installed for 56 days (August to October 2021) at two field plots with contrasting dissolved HS^- concentrations (see Section S1.1 for further information). Both field plots were located in the intertidal flat of Friedrichskoog (Fig. S1), Schleswig-Holstein Wadden Sea National Park, Northern Germany. The low-sulfide plot was an intertidal flat and characterized by low aqueous HS^- concentrations (≤ 50 μM, Fig. 1I). While located only 5 m away, the high sulfide plot was situated in the transition zone between the salt marsh and the intertidal zone (Fig. S2) and had dissolved HS^- concentrations of up to 6.7 mM (Fig. 1J).

A metal rod (diameter ~ 1 cm) was used to make a hole (15 cm deep) in the sediment for sample installation during low tide. A 30 cm long PVC core-liner (UWITEC, 8.6 cm diameter) was then pushed into the sediment (3 cm deep) around the hole. The inner volume of the PVC core-liner was flushed with N_2 for several minutes. Subsequently, the sample was removed from the air-tight double-sealed Al-bag and immediately pushed into the sediment under constant N_2 flow to avoid oxidation of the vivianite. Immediately after sample installation, no gap between the sediment and the nylon rod connected to the sample was visible (Fig. S4A, S5A). Four treatments in triplicate were deployed within each field plot (Fig. S4, S5).

2.2.2. Porewater monitoring

Approximately every 7 to 10 days during the field experiment, sediment temperature (at ~ 10 cm depth) and oxidation-reduction potential (ORP) were measured at both field plots during low tide (± 3 h). Sediment temperature was recorded in the center of the field plots. ORP was determined with a custom-made ORP probe with Pt electrodes at depths of 0, 4, 9, 14, 19, 24, 29, and 34 cm and an AgCl-reference electrode (supersaturated KCl, Paleo Terra, The Netherlands). At the high sulfide plot, ORP was also recorded in the center of the field plot, while at the low sulfide plot, the electrode was installed ~ 2 m from the center of the sample assembly. After 1 h of stabilization time, ORP values were measured and converted to redox potentials (Eh) relative to the standard hydrogen electrode (+204 mV at 20 °C, Striggow, 2017).

We also collected pore water samples for chemical characterization on days of temperature and Eh monitoring. MacroRhizons (Rhizosphere, The Netherlands) with a 5 cm long porous tip (outer diameter 4.5 mm, 0.15 μm pore size) were inserted into the sediment in the center of a set of four samples (total three MacroRhizons per field plot, Fig. S4) to collect porewater from a sediment depth of 15 to 20 cm, matching the burial depth of the samples. The first 2 mL of porewater was discarded to clean the MacroRhizons and remove any O_2 from the tubing. Afterward, porewater was collected for major element and anion analysis, HS^-, pH, and alkalinity. First, for major elemental analysis, ~ 3 mL of porewater was collected directly into pre-acidified (30 μL ultra-high purity, concentrated nitric acid), N_2-flushed and pre-vacuumed crimp vials to avoid oxidation of oxygen-sensitive species. The samples were stored at 4 °C until analysis. Secondly, N_2-flushed and pre-vacuumed crimp vials containing 2 mL of 2% zinc acetate solution were connected

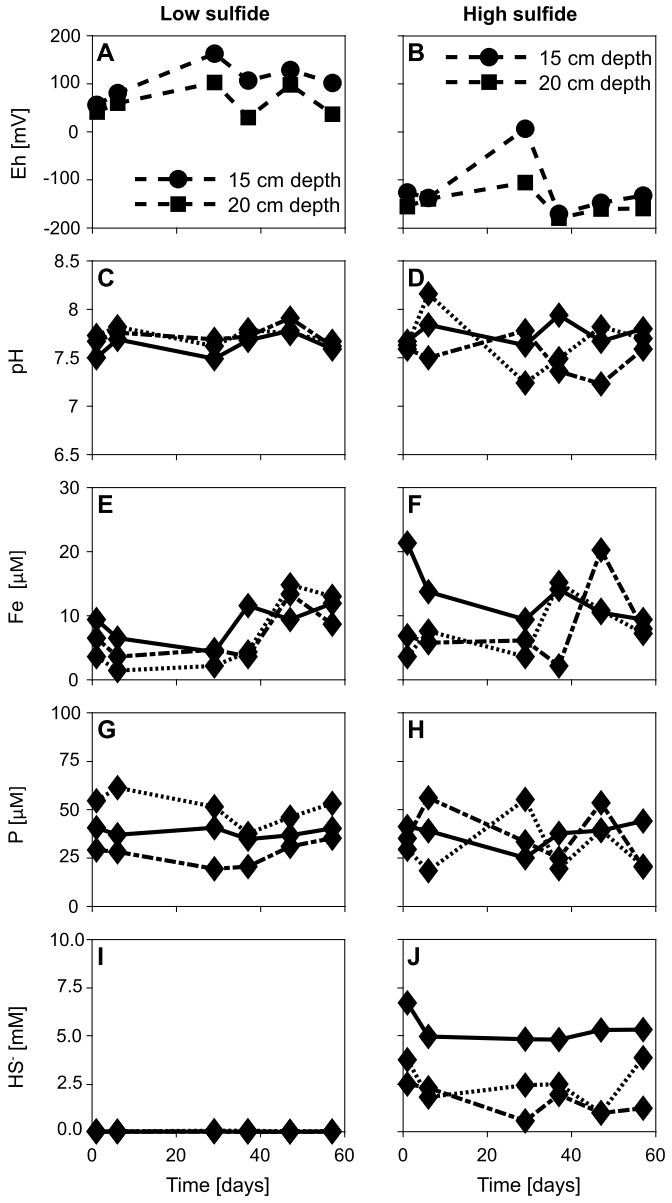

Fig. 1. Temporal changes in Eh (AB), pH (CD), dissolved Fe (EF), dissolved P (GH), and HS^- (IJ) at the low and high sulfide field plot during the experimental period. Eh (AB) was measured in-situ at 15 and 20 cm depth at both field plots. Porewater samples were collected at 17.5 cm sediment depth at three different locations within the experimental plot represented by the three different lines in panels C to J. A re-scaled figure of panel I showing the low HS^- concentrations is illustrated in Fig. S12.

to collect ~ 0.5 mL of porewater for HS^- analysis. The samples were also stored at 4 °C until analysis. Exact porewater volumes were determined gravimetrically after sample collection. For major anion, pH, and alkalinity analyses, porewater was directly collected into a N_2-flushed, pre-vacuumed crimp vial. The crimp vials were opened and pH measured (double-junction electrode, 3 M KCl, Metrohm AG, Switzerland) less than 6 h after porewater extraction. A 2 mL aliquot of the porewater sample was taken for alkalinity titration using 0.01 M HCl via a two-step titration (Titrimetric test kit, VISOCOLOR HE Carbonate hardness, Macherey-Nagel). Another subsample (0.5 mL) was taken for major anion analysis and frozen (-20 °C) until further analysis. Porewater depth profiles were collected for additional plot characterization at the end of the field experiment (see Section S1.5). Additionally, passive DGT samplers for dissolved sulfide species (binding layer of AgI, DGT® Research) were installed at three time points across the duration of the field experiment to gain insights into the temporal and (micro)spatial heterogeneity regarding dissolved HS^- content at the two field plots (see Section S1.5).

2.2.3. Processing of samples

After 56 days, all samplers were still in place at the field plots, and there were no signs of erosion of sediment (Fig. S4, S5). Sample holders were pulled out and cut from the nylon rods and were immediately vacuum sealed (Fosa Vacuum bags, Malaga series) and stored on ice. Wet sediment covered the retrieved sample holders, which additionally likely helped to prevent oxidation of the samples (Fig. S7). A sediment sample (~ 50 g) at each field plot was taken from a depth of 15 to 20 cm for solid-phase characterization of the field plots (further information in Section S1.3).

In less than 3 h, recovered sample holders and sediment samples were additionally sealed in air-tight, N_2-flushed double-sealed Al-bags containing O_2 adsorbers and frozen at -20 °C. Samples were transported in sealed bags, on ice, back to the laboratory at ETH Zürich, where they were dried under N_2 atmosphere and further processed in an anoxic chamber. Drying was achieved in less than 3 days. After drying, the surrounding sediment was removed from the sample holders, and the mesh bags were carefully recovered. The content of the mesh bags (~ 1 g) was gently homogenized by hand with an agate mortar and pestle. A sub-sample (~ 200 mg) was further milled by hand with mortar and pestle to a grain size of less than ~ 100 µm. The homogenized and milled samples were stored in air-tight, amber glass vials in the anoxic chamber until further processing.

2.3. Porewater analysis

Pre-acidified samples were analyzed by ICP-OES for major dissolved elements (Ca, Mg, Fe, Mn, K, Na, Si, P, S). Dissolved sulfides were determined spectrophotometrically using the methylene blue protocol (Cline, 1969). Frozen samples for major anion analysis were thawed and analyzed for Cl^-, Br^-, F^-, and SO_4^{2-} using ion chromatography (IC, Metrohm 940 Professional IC Vario). Elemental porewater concentrations, Eh, pH, alkalinity, and temperature were used to calculate mineral saturation indices for the porewater using Visual MINTEQ (Version 3.1, Section S1.6).

2.4. Solid phase analysis

2.4.1. Sediment samples

The sediment collected from each field plot was analyzed for its total elemental contents. For this, a representative sub-sample of each field plot was milled with a vibratory disc mill (Retsch). Subsequently, the total element contents were measured by X-ray fluorescence (XRF, XEPOS, Spectro, Germany) using pressed pellets of milled samples. To gain further information on the Fe-speciation of the two field plots, ~ 100 mg of homogenized, dried sediment samples were subjected to a six-step sequential extraction based on a combination of Poulton and Canfield (2005) and Claff et al. (2010) (see Section S1.4 for further information). In addition to carrying out Fe sequential extraction on the sediment samples, for both sediment samples ^{57}Fe-Mössbauer spectra were collected using a ^{57}Co/Rhγ-radiation source in constant acceleration mode in transmission setup (WissEl, Wissenschaftliche Elektronik GmbH). ^{57}Fe-Mössbauer spectra were collected at 77 and 5 K inside a closed-cycle exchange gas (He) cryostat (SHI-850, Janis Research Co.; further information on sample preparation and analysis can be found in Section S1.4).

2.4.2. Elemental composition and changes in reacted samples

The reacted samples changed color from white-grayish to dark blue, dark green, and black, pointing towards a change in mineralogy. The mineral phases in a subsample of the homogenized, dried, non-milled reacted mineral-sand mixes (~ 50 mg, in duplicate) were dissolved in

10 mL of 6 M HCl overnight to determine the bulk elemental composition. After acid addition, the remaining solid phase looked like the initial sea sand. To prevent the escape of volatilized hydrogen sulfide, samples were immediately capped after acid addition, and no smell of hydrogen sulfide was detected. Nevertheless, some undetected escape of volatilized hydrogen sulfide could have still occurred, potentially leading to slight underestimations of the determined solid-phase S concentrations. To minimize losses, samples were immediately analyzed and only decapped directly prior to analysis. The supernatants (filtered, 0.22 μm nylon) were analyzed by ICP-OES for Fe, Mn, Mg, Ca, P, and S.

The results of the bulk elemental analysis were used to derive changes in elemental composition (in mmol/g) during the field experiment compared to the nominal initial concentrations. Using the absolute changes in comparison to the initial concentrations, we calculated % losses of Fe, Mg, Mg, Ca, and P, assuming that changes were caused by mineral dissolution rather than mechanical loss. We performed the Mann-Whitney U test in MATLAB to assess whether elemental losses and gains in the reacted samples were significantly different between treatments and field plots (further information in Supplementary Material, Section S1.7). We chose the Mann-Whitney U test because it does not assume a normal distribution and remains robust with small sample sizes.

2.4.3. Fe, P, and S speciation

Bulk Fe K-edge XAS spectra were collected at the Balder beamline of MAX IV synchrotron (Lund, Sweden), and P and S K-edge X-ray absorption near edge structure (XANES) spectra were collected at the PHOENIX beamline of the Swiss Light Source (PSI, Switzerland) for reacted samples.

All Fe, P, and S K-edge XAS spectra were energy calibrated, pre-edge subtracted, and post-edge normalized in Athena (Ravel and Newville, 2005). For Fe and P, the edge energy, E_0, was defined as the maximum peak in the first XANES derivative. Sulfur spectra were normalized to the absorption at 2490 eV. Normalized Fe K-edge extended X-ray absorption fine structure (EXAFS) spectra and P K-edge XANES spectra were analyzed by linear combination fitting (LCF; further details on sample preparation and data analysis are presented in Sections S1.8 and S1.10). Bulk Fe K-edge XAS spectra were measured and analyzed for each replicate sample from each treatment and field plot individually. Averaged fitted mineral fractions and associated standard deviations were then calculated for each treatment and field plot. In addition to Fe K-edge XAS analysis, solid-phase Fe speciation was also investigated by ^{57}Fe-Mössbauer spectroscopy for reacted samples (Supplementary Material, Section S1.9).

Normalized S K-edge XANES spectra were deconvoluted using WinXAS V4.0 (Ressler, 1998). Deconvolution included a set of up to eight Gaussians for the S s->p transition peaks and one arctangent at ~ 2475 eV representing the post-edge absorption of 'reduced' S species and a second arctangent at >2489 eV representing the post-edge absorption of 'oxidized' S species. The peak energy of the white lines of the S K-edge XANES spectrum shows a linear relationship with the oxidation state of the S atom. Hence, each fitted Gaussian line represents another oxidation state of the S atom (Manceau and Nagy, 2012). The areas of the fitted Gaussians were calculated and subsequently corrected for the oxidation state-dependent change in absorption cross-section, following a linear increase with the oxidation state of the S atom, based on the generic curve presented by Manceau and Nagy (2012). To subsequently determine the relative contribution of every S species to the total S in the sample, the corrected peak area for each S species was normalized to the peak-area sum of all identified S species (see Section S1.11 for further information).

2.4.4. Synchrotron based μ-XRF mapping

μ-XRF maps were collected at the PHOENIX beamline of the Swiss Light Source (PSI, Switzerland). Maps were collected for one sample of each treatment incubated at the high sulfide field plot to gain information on the spatial elemental distribution. The samples used for the collection of the μ-XRF maps were identical to the samples used for the collection of the bulk P K-edge XANES spectra. XRF spectra were collected at room temperature using a mono-element detector (Silicon drift diode). A focused beam with a diameter size of 5 μm at an energy of 7250 eV was used. Mapping was conducted over an area of 200 x 160 μm with a step size of 5 μm and a dwell time of 2 s. The collected spectra were processed and converted to elemental maps using PyMCA Toolkit (Solé et al., 2007), and Pearson elemental correlation coefficients were calculated in MATLAB.

3. Results

3.1. Geochemistry of the two field plots

The sediments sampled at 15 to 20 cm depth at both field plots exhibited similar solid phase composition (Table S4). However, despite only a 5 m distance between the two field plots, certain differences existed, particularly regarding solid phase S content and solid phase Fe speciation. Solid phase S content was lower at the low sulfide plot in comparison to the high sulfide plot (108 versus 183 μmol/g, respectively). Both field plots had comparable total Fe contents (181 to 194 μmol/g, Table S4) at 15 to 20 cm depth. However, the sum of sequentially extracted Fe varied among the sediment samples (Sections S1.4, Table S4, S5, Fig. S9). Additionally, the percentage contribution of Fe extracted from each fraction differed for the two sediment samples (Fig. S9), suggesting different mineralogy across the two field plots.

At the low sulfide plot, 30% (~ 50 μmol/g) of the solid-phase Fe was extractable by the six-step sequential Fe extraction. Most of the Fe was extracted by sodium acetate (Step 2), hydroxylamine hydrochloride (Step 3) and citrate dithionite bicarbonate (Step 4; Fig. S9, see Section S1.4), suggesting the presence of reactive Fe-mineral phases and iron(oxyhydr)oxides (Poulton et al., 2004). The fitted hyperfine parameters of a present sextet in the ^{57}Fe-Mössbauer spectra at 77 K and 5 K (Fig. S10, Table S6) matched a mix of iron(oxyhydr)oxides such as goethite, lepidocrocite, and ferrihydrite (Notini et al., 2022, 2023). Due to noise, it was not possible to identify unambiguously the present iron(oxyhydr)oxide mineral. Collectively, the sequential Fe extraction and ^{57}Fe-Mössbauer spectroscopy both indicate the presence of iron(oxyhydr)oxides at the low sulfide plot.

At the high sulfide plot, 41% (~ 60 μmol/g) of the solid-phase Fe was extractable by the six-step sequential Fe extraction. Nearly 60% of the extractable Fe was extracted by HNO_3 (Step 6), targeting pyrite and thus suggesting the presence of pyrite at the high sulfide plot (Fig. S9). This result matched the darker color of the sediment (Fig. S3) and the high dissolved HS^- concentration. In addition, the ^{57}Fe-Mössbauer spectrum of the sediment collected at 77 K was fitted with two doublets and one sextet (Fig. S10, Table S6). One doublet (Fe(II)D1) was compatible with various phyllosilicate clays (Vandenberghe and De Grave, 2012), adsorbed Fe(II) (ThomasArrigo et al., 2017), and other reduced Fe-minerals such as ferrous oxide and green rust (Mackey and Collins, 1967; Génin et al., 1998; Kukkadapu et al., 2004). The second doublet had a quadrupole splitting value of 0.55 mm s^{-1}, aligning with Fe(III) bound in green rust and/or pyrite (Kukkadapu et al., 2004; Thiel et al., 2019). The hyperfine parameters of the sextet (FeSx) matched values reported for Fe-sulfide minerals (Thiel et al., 2019). Collectively, the results of the sequential Fe extraction and ^{57}Fe-Mössbauer spectroscopy indicate the presence of pyrite and Fe-sulfide minerals at the high sulfide plot.

The low sulfide plot was characterized by positive Eh values (40 to 200 mV, Fig. 1) at 15 to 20 cm depth during low tide and pH values varied between 7.5 and 8.0 during the field experiment. Dissolved Fe in the porewater was low with concentrations not exceeding 20 μM. Dissolved P concentrations were generally higher than dissolved Fe with values ranging around 25 to 50 μM. Concentrations of HS^- exhibited high spatial variability and ranged from 0 to 50 μM.

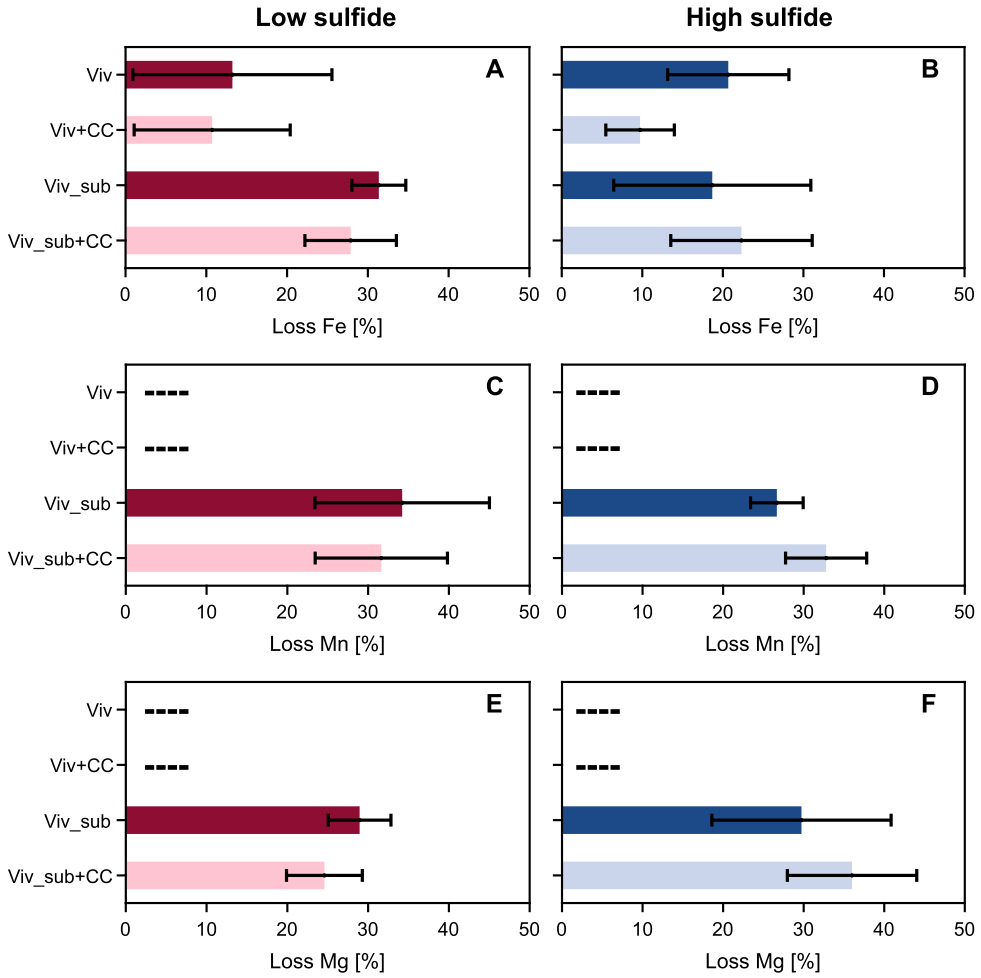

Fig. 2. Changes in solid-phase Fe (AB), Mn (CD), and Mg (EF) content in the mesh bags during the field experiment determined by 6M HCl acid digestion followed by ICP-OES measurements. No Mn or Mg was detected in samples of Viv and Viv+CC after the field experiment as indicated by — in Panels C-F. Changes are presented in % losses and error bars indicate the standard deviation derived from the incubated triplicates per treatment and plot. Absolute changes [in mmol/g] are presented in Table S11.

In contrast to the low sulfide plot, the high sulfide plot was characterized by more negative Eh values (-200 to 0 mV, Fig. 1) at 15 to 20 cm depth for the duration of the experiment. While Eh differed strongly, pH, dissolved Fe and P concentrations were comparable between the two field plots. However, HS^- concentrations ranged between 0.6 to 6.7 mM at the high sulfide plot and were thus ~ 100 times higher at the high sulfide plot than at the low sulfide plot.

The porewater composition was used to perform chemical equilibrium calculations to investigate the saturation state of the porewater with respect to various mineral phases (Tables S7 to S10). The porewater at 15 to 20 cm depth at both field plots was undersaturated with respect to vivianite (range of saturation indices: -11.2 to -1.7). Saturation indices for mackinawite varied with time and sampling location between -0.6 to 0.4 at 15 to 20 cm depth at the low sulfide plot, while the porewater at the high sulfide plot was mainly oversaturated with respect to mackinawite (range of saturation indices: 0 to 0.9, two outliers below 0).

3.2. Changes in metal content and speciation of reacted samples

Our thermodynamic calculations predict that vivianite was unstable in both field plots at 15 to 20 cm sediment depth (Table S7-S10). This agrees well with an overall loss of solid-phase Fe through mineral dissolution from the mesh bags for all treatments and both field plots (Fig. 2AB, Table S11). At the low sulfide plot, between ~ 10 and 31% of solid-phase Fe was lost. Losses in solid-phase Fe were significantly lower ($p = 0.009$) for Viv+CC and Viv treatments than for Viv_sub+CC and Viv_sub treatments (10 to 13% versus 28 to 31% loss, respectively) at the low sulfide plot (Table S11). The presence of $CaCO_3$ tended to slightly lower solid-phase Fe loss (Table S12). However, the standard deviation among samples with $CaCO_3$ was larger than the differences among treatments.

At the high sulfide plot, losses in solid-phase Fe ranged from ~ 10 to 22% across all treatments (Fig. 2B, Table S11) and were thus slightly but not significantly lower than at the low sulfide plot ($p = 0.589$, $p = 0.180$; Table S16). Similarly to the low sulfide plot, substitution in the vivianite (treatments Viv_sub and Viv_sub+CC) resulted in a moderately higher solid-phase Fe loss, which, however, was not statistically significant ($p = 0.240$). The presence of $CaCO_3$ lowered Fe loss for Viv+CC in comparison to Viv treatment ($p = 0.1$), while no effect was detectable for treatments containing Viv_sub ($p = 0.7$).

Incubation of Viv_sub and Viv_sub+CC also resulted in a loss of solid-phase Mn and Mg (Fig. 2C-F, Table S11). Losses in solid-phase Mn and Mg ranged between 25 to 36% (Fig. 2CD) and were generally slightly higher than solid-phase Fe losses for the same treatment and field plot. Losses of Mg were significantly higher ($p = 0.065$) than losses in Fe from Viv_sub and Viv_sub+CC at the high sulfide plot, respectively (Table S14).

Changes in Fe speciation in the samples after the field experiment were assessed by LCF of the k^3-weighted Fe K-edge EXAFS spectra, as well as by ^{57}Fe-Mössbauer spectroscopy (see Section S2.5). Fe K-edge EXAFS spectra were collected for each replicate individually and the

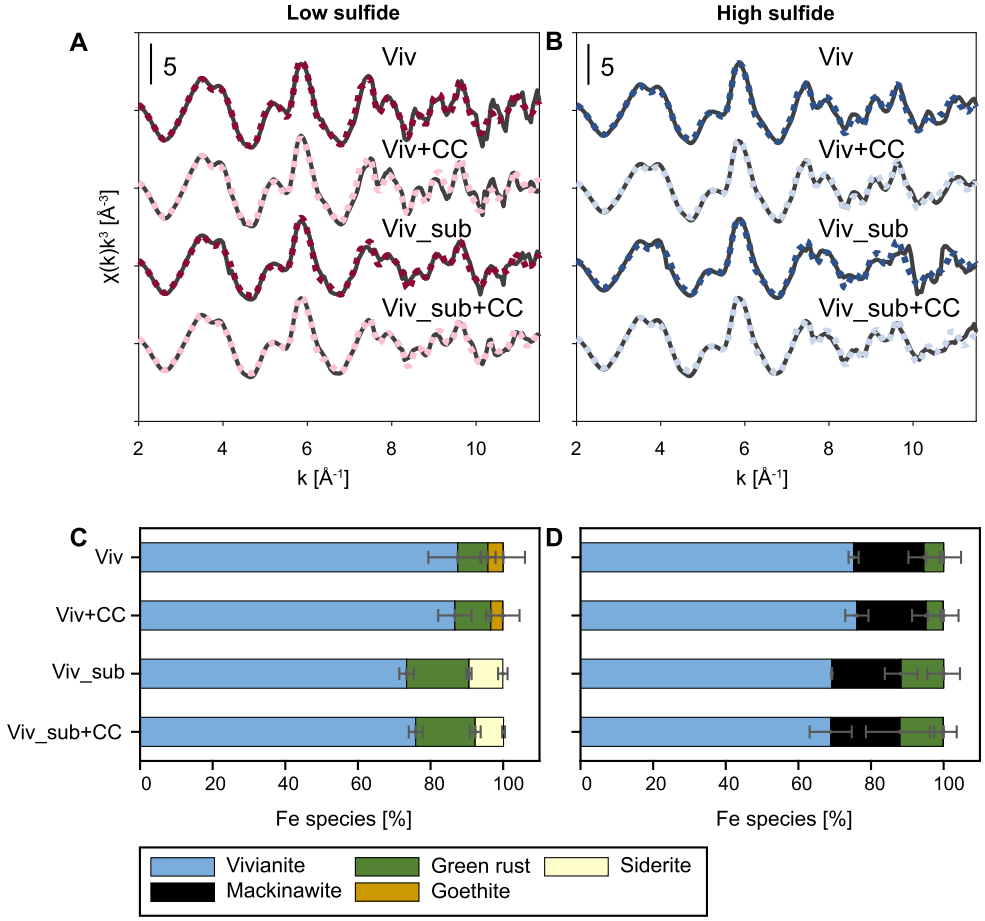

Fig. 3. Examples of Fe K-edge EXAFS spectra of each treatment and field plot (AB). Solid lines indicate experimental data and dotted lines show the LCF. All collected Fe K-edge EXAFS spectra with their respective fit are presented in Fig. S30. Averaged mineral fractions and associated standard deviations (CD) were determined from the fitted fractions of the replicates of the same treatment and field plot. Table S27 and S26 present the individual LCF and the average LCF fit results, respectively.

fitted fractions were then averaged per treatment and field plot. At the low sulfide plot, most of the remaining Fe was identified as vivianite based on LCF analysis (Fig. 3AC). For Viv and Viv+CC treatments, on average ~ 85% of Fe was fitted as vivianite. The remaining Fe was present as green rust (a carbonate green rust was used as a reference, see Section S1.8) and goethite (on average ~ 9 and ~ 4%, respectively). Less Fe was fitted as vivianite for Viv_sub and Viv_sub+CC treatments (on average ~ 74%), while the contribution of green rust and siderite was enhanced (on average ~ 17 and ~ 8%, respectively). Interestingly, siderite was only detected for treatments containing Mn and Mg.

Results of the LCF of the k^3-weighted Fe K-edge EXAFS spectra at the high sulfide plot showed similar trends among all treatments (Fig. 3BD). No goethite or siderite was fitted, while mackinawite was present in all samples. In the case of the Viv and Viv+CC treatments, on average ~ 75% of Fe was fitted as vivianite, followed by ~ 19% bound in the form of mackinawite and ~ 5% as green rust. Similar to the low sulfide plot, the fraction of Fe bound in the form of vivianite for Viv_sub and Viv_sub+CC was smaller with an average ~ 68% than for the Viv and Viv+CC treatments. Mackinawite was the second most abundant Fe phase (on average ~ 19%), followed by green rust (on average ~ 12%). Results of ^{57}Fe-Mössbauer spectroscopy at 77 K additionally suggested the presence of a disordered FeS_x phase at the high sulfide plot (Thiel et al., 2019, Section S2.5).

3.3. Changes in P content and speciation

Similar to solid-phase Fe, Mn, and Mg losses, solid-phase P was lost from the reacted samples for all treatments and both field plots (Fig. 4AB). Between ~ 9 and 33% of solid-phase P was lost at the low sulfide plot. Losses were significantly higher for Viv_sub+CC and Viv_sub treatments than for Viv+CC and Viv treatments at the low sulfide plot ($p = 0.002$; 27 to 33% loss versus 9 to 12% loss, respectively, Table S15). The presence of $CaCO_3$ tended to lower the loss of P; however, this effect was not statistically significant (Table S12).

At the high sulfide plot, losses of solid-phase P were significantly higher than at the low sulfide plot for Viv and Viv+CC treatment ($p = 0.026$; 32% and 18% loss), while the loss was only moderately higher for Viv_sub and Viv_sub+CC treatments ($p = 0.669$; 28% and 31% loss, Table S16). The reacted samples had a greater molar ratio of (Fe+Mn+Mg)/P than the initial samples (increases up to 1.94, initial ratio 1.66 for Viv, Table S11), indicating a preferential loss of P over Fe from the reacted samples (Table S14), likely related to mineral transformations which retained Fe but not P. At the high sulfide plot, the presence of $CaCO_3$ lowered the solid-phase P losses, particularly for Viv treatments ($p = 0.1$; Table S12). Smaller increases in molar ratios of (Fe+Mn+Mg)/P for treatments with $CaCO_3$ at the high sulfide plot suggest further that solid-phase P was better retained in those samples (Table S11).

P K-edge XANES spectra were fitted by LCF to determine the speciation of the remaining solid-phase P in field-reacted samples (Fig. 4C-F, S27, Table S24). While differences in P loss were detected depending on the field plot, the P speciation was similar between the same treatments incubated at the different field plots. The majority of the solid-phase P for Viv and Viv+CC treatments was fitted as vivianite (~ 70 to ~ 85%).

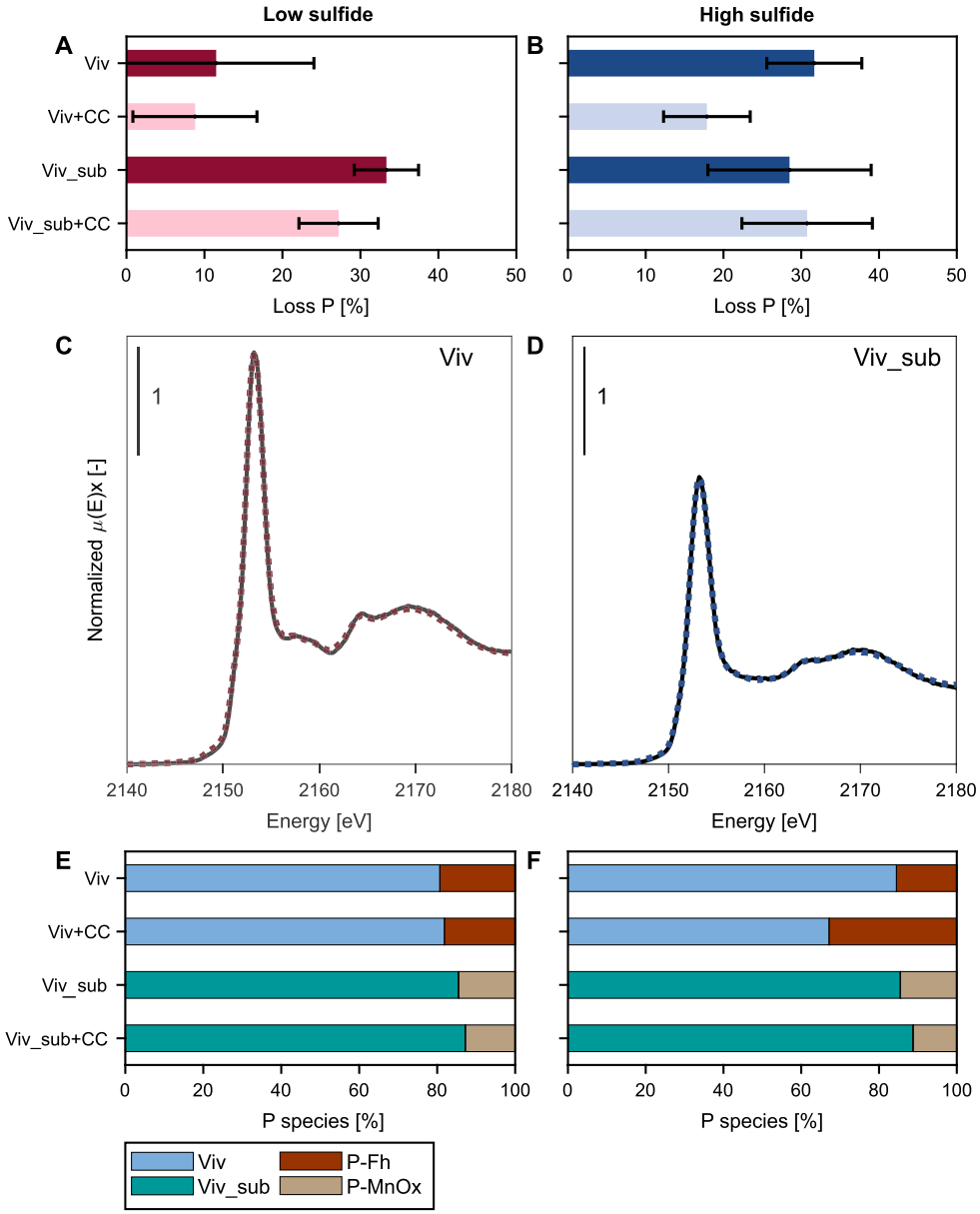

Fig. 4. Changes in solid-phase P content (AB) in the mesh bags during the field experiment determined by acid digestion followed by ICP-OES measurements. Changes are presented in losses and error bars indicate the standard deviation derived from the incubated triplicates per treatment and plot. The error bar for Viv (Subfigure A) is larger than the limits of the y-axis and thus not visible. Absolute changes [in mmol/g] are presented in Table S11. Examples of fitted P K-edge XANES spectra (CD). Solid lines indicate the normalized experimental data, and dotted lines show the LCF fit. All fitted P K-edge XANES spectra, used references, and LCF results are presented in Fig. S27, S28 and Table S24. Mineral fractions (EF) determined by LCF of the P K-edge XANES spectra.

The remaining P was associated with ferric iron minerals (modeled by P adsorbed to ferrihydrite (P-Fh)).

In the case of Viv_sub and Viv_sub+CC treatments, most of the P was fitted as Mn-Mg-substituted vivianite (~ 85 to ~ 88%) after incubation at both field plots. The remaining P was mainly present as P associated with Mn-oxide phases (adsorbed or co-precipitated with), highlighting a change of P secondary mineral formation due to the initial cation substitution in vivianite. However, it should be noted that using P-Fh in the LCF instead of P-MnOx only slightly decreased the fit quality (compare Table S24 with S25). As it is difficult to differentiate between P associated with ferric minerals and Mn-oxides based on P K-edge XANES, we hypothesize that P was potentially associated with a mixture of both (see Section S1.10 for further information). This hypothesis is further supported by a positive correlation between the spatial distribution of P, Fe and Mn based on μXRF maps collected for samples from the high sulfide plot (Fig. S36, S38). Fe and Mn were strongly positively correlated for Viv_sub and Viv_sub+CC treatments (Pearson correlation coefficient = 0.8 and 0.7, respectively, Table S30, S31). The correlation between P and Mn (Pearson correlation coefficient = 0.5 and 0.4) was generally stronger than for P and Fe (0.4 and 0.2) for Viv_sub and Viv_sub+CC treatments, respectively, suggesting that P was likely associated with a Mn- and Fe-phase. While LCF of the P K-edge XANES did not indicate the presence of P associated with Ca even in the presence of $CaCO_3$, μXRF maps collected on the incubated samples showed a weak positive correlation between P and Ca (0.2 for Viv and 0.13 for Viv_sub, Table S29, S31), pointing towards the association of P with Ca.

3.4. Changes in S content and speciation

In contrast to the solid-phase loss of Fe, Mn, Mg, and P from the reacted samples, S accumulated in the solid-phase during the field experiment, indicating the formation of a mineral phase containing S

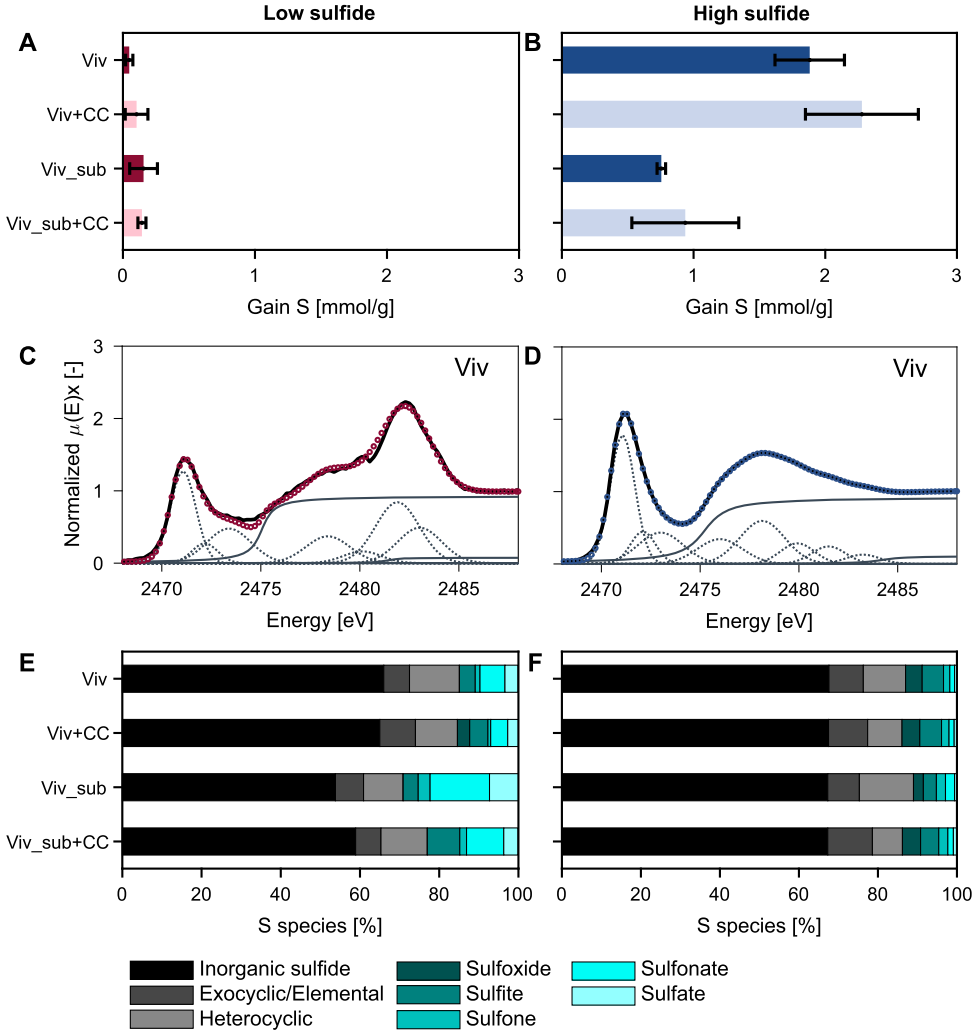

Fig. 5. Changes in solid-phase S content (AB) in the mesh bags during the field experiment determined by acid digestion followed by ICP-OES measurements. Note that due to potentially undetected sulfide volatilization during acid digestion, S contents might be underestimated. Examples of the deconvolution of normalized S K-edge XANES spectra (CD). Solid black lines indicate the normalized experimental data and dotted lines show the sum of the deconvolution fit. Samples were decomposed into seven to eight Gaussians and two arctangent functions. All deconvolutions of normalized S K-edge XANES spectra are presented in Fig. S26. Determined S speciation fractions for each treatment and field plot (EF), which was determined by the deconvolution of the S K-edge XANES spectra.

(Fig. 5). Only very little solid-phase S was gained at the low sulfide plot (less than 0.2 mmol/g, Fig. 5A). In contrast, substantial amounts of solid-phase S accumulated in the samples at the high sulfide plot (0.8 to 2.3 mmol/g, Fig. 5B, Table S11). Significant differences between treatments were present (Table S17). For example, the gain in solid-phase S was twice as high in Viv and Viv+CC treatments compared to the Viv_sub and Viv_sub+CC treatments (up to ~ 2.3 vs. ~ 0.9 mmol/g, respectively), indicating that S better accumulated in treatments containing Viv than Viv_sub, possibly due to increased secondary mineral formation. Solid-phase S was generally homogeneously distributed in the solid-phase as indicated by synchrotron-based μXRF-mapping (Fig. S31 to S37), with only minor hot spots present.

Deconvolution of S K-edge XANES spectra was used to gain information on the oxidation state of the present solid-phase S in the reacted samples. For all treatments, seven to eight Gaussian functions and two arctangent functions (background for reduced and oxidized species) were fitted per S K-edge XANES spectra (Fig. 5CD, S26). For all treatments at the low sulfide plot, the dominant S species was inorganic sulfide (54 to 66%, Fig. 5E, Table S21), followed by exocyclic/elemental S, heterocyclic S, and sulfonate. The reduced to oxidized species ratio ranged from 2.4 to 5.8 (Table S23). Reduced S species were considered to be inorganic sulfide, exocyclic/elemental S, and heterocyclic S, while the remaining S species were defined as oxidized.

Similar to the low sulfide plot, inorganic sulfide was the dominant S species (~ 67%, Fig. 5F, Table S22) for all treatments at the high sulfide plot, followed by exocyclic/elemental S and heterocyclic S. Ratios of reduced to oxidized S species ranged from 6.2 to 8.0 and were thus elevated at the high sulfide plot compared to the low sulfide plot, highlighting the presence of more reduced S species at the high sulfide plot (Table S23).

4. Discussion

4.1. Geochemical conditions drive differences in transformation products

The overall loss of elements associated with the initial vivianites (Fe, Mn, Mg, and P) matches our thermodynamic calculations, predicting that vivianite was unstable in both field plots. Elemental loss points towards the dissolution of vivianite with subsequent diffusive and advective transport of elements out of the mesh bags into the surrounding environment. An overall loss of solid-phase elements further suggests that secondary mineral formation could not retain all elements released upon vivianite dissolution. We do not expect that substantial vivianite

was lost due to particle loss into the surrounding environment, as particle aggregation is favored at high ionic strength (Gunnars et al., 2002).

For all treatments and both field plots, most of the remaining solid-phase Fe was fitted as vivianite based on LCF of the Fe K-edge EXAFS spectra. This result differs from laboratory studies showing a complete dissolution and transformation of vivianite under oxidizing conditions within 28 to 53 days under air or CO_2-free O_2 conditions (Roldán et al., 2002) and sulfidic conditions (1 to 500 mM) within 4 to 100 h (Dijkstra et al., 2018; Wilfert et al., 2020). Hence, our results suggest that either vivianite dissolution kinetics are slower under field conditions or complete dissolution is inhibited. We speculate that multiple mechanisms may be responsible for this, which we elaborate on in the following section. The formed secondary minerals might have potentially developed as a protective layer around the vivianite crystals, protecting the inner core of the crystal from further dissolution. For instance, mackinawite oxidation at neutral to basic pH, as present at both of our field plots, may result in the development of an iron(oxyhydr)oxide coating on the mackinawite surface, which could inhibit further solid-phase oxidation (Jeong et al., 2010). Similarly, the precipitation of mackinawite or FeS_x on the surface of iron(oxyhydr)oxides can slow down sulfidation (Poulton et al., 2004). In addition to a positive correlation between S and P, the homogeneous distribution of solid-phase S, as determined by synchrotron-based μXRF-mapping, likely supports the hypothesis of the formation of Fe-sulfide minerals as a protective layer around vivianite crystals (Fig. S31 to S38, Table S28 to S31). Thus, we hypothesize that the precipitation of secondary minerals upon vivianite dissolution on the crystal's surface may protect vivianite from further reaction. Further investigation by, for instance, electron microscopy would be needed to identify such a protective layer unambiguously.

Moreover, in natural sediments, vivianite is present in a sediment matrix with higher solid-to-solution ratios compared to model systems. We imitated such a system by mixing the vivianites with sea sand. Thus, our set-up was likely diffusion-limited in comparison to laboratory experiments with mixed suspensions. Thus, vivianite dissolution caused by the diffusion of dissolved HS^- into the mesh bags, followed by secondary mineral formation, could have been slowed down. Overall, our results indicate slower in-situ dissolution and transformation kinetics of vivianite than observed in well-mixed slurry experiments. This result suggests that vivianite crystals in the environment can persist for some time period prior to complete dissolution and transformation and, thus, might not act as a source of bioavailable phosphate during short-term environmental perturbations. Additionally, our results provide novel insights into the transformation products of partial vivianite transformation under contrasting geochemical conditions, which will be discussed in detail in the following.

4.1.1. Transformation products at low sulfide plot

The low sulfide plot was characterized by lower dissolved HS^- concentrations and positive Eh values during porewater monitoring (Fig. 1). Eh values of 40 to a maximum of 200 mV represent anoxic to suboxic conditions under which ferric iron reduction may occur (Grundl et al., 2011). Despite moderately reducing conditions during low tide and likely more reducing conditions during high tide, the bulk porewater was undersaturated with respect to vivianite (Table S7, S8) due to low dissolved Fe and P concentrations (Fig. 1). Thus, the undersaturation of the porewater with respect to vivianite resulted in the dissolution of vivianite, with subsequent partial formation of secondary minerals. Using an anion exchange resin to remove any released phosphate, Roldán et al. (2002) showed that the oxidation through the addition of air or CO_2-free O_2 through bubbling resulted in the formation of lepidocrocite from an initial vivianite suspension with calcite sand. We did not observe the formation of lepidocrocite at the low sulfide plot. Instead, green rust and minor amounts of goethite and siderite were formed. Siderite was only detected in treatments containing Viv_sub and its formation is further discussed in Section 4.2. Green rust, an Fe(II-III) layered double hydroxide, is an intermediate transformation product during the partial oxidation of dissolved ferrous iron at circumneutral pH before crystalline iron(oxyhydr)oxide formation (e.g., Schwertmann and Fechter, 1994). Thus, the formation of green rust suggests that vivianite dissolution followed by oxidation of the released Fe(II) was the dominant transformation pathway at the low sulfide plot. The formed green rust could either be a sulfate or carbonate green rust. We hypothesize that a carbonate green rust formed, as carbonate usually outcompetes sulfate for green rust formation (Refait et al., 1997). However, using Fe K-edge XAS data alone, we cannot distinguish between the two different types of green rust (Refait et al., 2001). Low ferric iron contents (determined by ^{57}Fe-Mössbauer spectroscopy, Fig. S21, S22) indicate inhibited oxidation and transformation rates of green rust to more stable iron(oxyhydr)oxide minerals. High local phosphate concentrations and subsequent phosphate sorption to green rust might have stabilized the mineral (Benali et al., 2001; Refait et al., 2007; Sahoo et al., 2011; Xiong et al., 2023). Phosphate adsorbed on the lateral faces of carbonate green rust has been shown to slow down carbonate release and thus green rust transformation (Bocher et al., 2004). Overall, suboxic conditions dominating at the low sulfide plot, coupled with high local phosphate concentration resulting from vivianite dissolution, may have stabilized the formed green rust from further transformation and could explain the absence of more crystalline iron(oxyhydr)oxides.

Results of LCF of P K-edge XANES suggest that up to 20% of solid-phase P was associated with ferric or manganese oxides or a mixture of both (see Section S1.10 for further information). Within these categories, we cannot specify the specific sorbent phase based on P K-edge XANES analysis. However, it would be plausible that P was associated with other iron(oxyhydr)oxides, as well as the formed green rust. Additionally, it is likely that amorphous $Fe(OH)_2$ precursors with adsorbed phosphate formed upon vivianite dissolution with similar Fe to P ratios as in vivianite (Xiong et al., 2023), which was not detected by Fe K-edge XAS. Those $Fe(OH)_2$ precursors would be very transient and easily oxidized, resulting potentially in the formation of green rust (Xiong et al., 2023). This formation mechanism would also explain the nearly unchanged molar ratios of (Fe+Mn+Mg)/P of the field-reacted samples at the low sulfide plot. Thus, overall, the secondary minerals formed upon vivianite dissolution under slightly reducing conditions were able to retain some of the released phosphates, implying that under those conditions, not all P released upon vivianite dissolution directly becomes bioavailable.

Sulfide-mediated dissolution of vivianite likely only played a minor role at the low sulfide plot. Only minor amounts of solid-phase S were gained inside the mesh bags during the field experiment (Fig. 5A). The presence of reduced sulfur species determined by S K-edge XANES analysis (Fig. 5CE) suggests the presence of minor amounts of FeS_x minerals. However, due to the low solid-phase S content, the fraction of solid-phase Fe present in FeS_x was below the detection limit of Fe K-edge XAS analysis (based on stoichiometric calculations FeS_x contributed not more than 7% to total Fe pool).

4.1.2. Transformation products at high sulfide plot

High dissolved HS^- concentrations and negative Eh values at the high sulfide plot suggest that sulfide-mediated vivianite dissolution was the major transformation pathway in this field plot. Sulfide-mediated vivianite dissolution is a surface-controlled reaction that does not involve changes in the oxidation state of the involved reactants (Equation (1)).

$$Fe_3(PO_4)_2 + 2HS^- \longrightarrow 2FeS + 2HPO_4^{2-} + Fe^{2+} \text{ (Bronner et al., 2023)} \quad (1)$$

The sulfide-mediated vivianite dissolution results in the formation of mackinawite, as has also been suggested by previous studies (Wilfert et al., 2020; Bronner et al., 2023). The LCF of the Fe K-edge analysis confirms that after 56 days of incubation, up to 20% of the solid-phase Fe was bound in the form of mackinawite. Additionally, S K-edge XANES indicated that up to 67% of the solid-phase S was present in the form of reduced inorganic sulfide. The fitted hyperfine parameters

of ^{57}Fe-Mössbauer spectra collected at 77 K suggest that reduced inorganic sulfide was present as a disordered FeS_x phase (see Section S2.5). Thus, LCF of the Fe K-edge analysis and ^{57}Fe-Mössbauer spectroscopy combined indicate the presence of mackinawite and/or disordered FeS_x phase. Overall, our results match previous observations showing that the reaction of ferrous iron and dissolved sulfide at low-temperature conditions results in poorly crystalline Fe-sulfide minerals such as mackinawite (Rickard et al., 1995; Rickard and Luther, 2007; Son et al., 2022). Despite the metastable nature of mackinawite, it can persist for long periods in reduced environments before transforming into more stable Fe-sulfide minerals such as greigite and pyrite (Berner, 1981; Benning et al., 2000; Rickard and Luther, 2007), which were not detected in our reacted samples.

The formation and presence of green rust in addition to FeS_x minerals inside the mesh bags suggest the occurrence of partial oxidation of either vivianite or the freshly formed FeS_x minerals (Jeong et al., 2010). However, the determined fraction of solid-phase Fe associated with green rust by LCF of the Fe K-edge EXAFS varied strongly between triplicates (Table S26, S27), indicating a strong spatial heterogeneity. The porewater at the high sulfide plot showed spatial and temporal variability as well, which could influence the transformation of vivianite in the mesh bags (Fig. 1, S14, S19). The high spatial variability might be related to the presence of rooted plants at the high sulfide field plot (Fig. S3, S5), which could result in a localized influx of minor amounts of O_2 (Howes and Teal, 1994).

The switch from ferruginous to euxinic conditions should increase the bioavailability of phosphate (Duverger et al., 2020; Alcott et al., 2022), as Fe-sulfide minerals are less efficient in adsorbing or co-precipitating P (Krom and Berner, 1980, 1981). The generally more extensive solid-phase P loss from the mesh bags incubated at the high sulfide plot than at the low sulfide plot supports this observation (Fig. 4AB) and indicates that vivianite dissolution under high sulfide conditions could weaken the sedimentary P retention capacity and may result in enhanced benthic P fluxes.

Most of the accumulated solid-phase S was present in a reduced phase (Fig. 5), while only minor amounts of oxidized solid-phase S were present at the high sulfide plot. Vivianite sulfidation does not result in changes in oxidation state of the involved reactants and thus does not lead to the formation of elemental sulfur or oxidized sulfur species as the sulfidation of iron(oxyhydr)oxides does (Pyzik and Sommer, 1981; Poulton et al., 2004). This likely explains the absence of a major oxidized solid-phase S pool. The minor amounts of oxidized solid-phase S could result from sample handling or could have diffused into the mesh bag from the surrounding environment, where abiotic sulfide oxidation is likely coupled to Fe and Mn reduction, resulting in the formation of polysulfides as well as oxidized sulfur species such as sulfate (Pyzik and Sommer, 1981; Schippers and Jørgensen, 2001).

4.2. Effect of cation substitution on vivianite transformation

Substitution of Fe by other cations may impact the sulfidation rates of various ferric and ferrous iron minerals and is likely dependent on the mineral and the incorporated cation. For instance, Wu et al. (2023) observed a slight hindering of the transformation of goethite to Fe-sulfides in the presence of Ni. In contrast, Poulton et al. (2004) showed an increase in sulfidation rate, expressed in terms of ferric content, of lepidocrocite with Al substitution. The increase was linked to a decrease in crystal size and, thus, an increase in surface area. Results of a laboratory suspension experiment by Dijkstra et al. (2018) suggested no difference in sulfide-induced dissolution kinetics between unsubstituted and Mn-Mg-substituted vivianite. However, the substituted vivianite contained a large fraction of struvite ($(NH_3)Mg(PO_4)\cdot 6\,H_2O$). Thus, it remained unclear how this second phase altered the results, and it was unknown how Mn and Mg substitution impacts in-situ vivianite transformation.

At the low sulfide plot, the oxidative transformation of vivianite dominated, evidenced by the presence of green rust. Substitution of Fe by Mn and/or Mg occurs preferentially in the double octahedron Fe position (Kubeneck et al., 2023). Redox-active atoms such as Mn and Fe can conduct homonuclear or heteronuclear intervalence electron transfer at this position (Allen and Hush, 1967), stabilizing vivianite against oxidative transformation (McCammon and Burns, 1980; Rouzies and Millet, 1993). With the incorporation of Mn and especially Mg, which does not participate in electron transfer with the Fe, this stabilization effect is likely altered and thus could impact the reactivity of vivianite in the presence of O_2 as hypothesized by Kubeneck et al. (2023). Significantly more P and Fe were lost upon vivianite dissolution from samples of the Viv_sub treatments than the Viv treatments at the low sulfide plot (Fig. 2, 4, Table S16, S15), suggesting that Viv_sub is more soluble under low sulfide conditions.

At high sulfide conditions, vivianite dissolution is controlled by sulfidation, a surface-controlled mechanism. Thus, decreases in crystal size and crystallinity, coupled with increases in crystal roughness as observed due to the incorporation of Mn and Mg in vivianite (Kubeneck et al., 2023), might enhance vivianite sulfidation, similar to trends observed by Poulton et al. (2004). However, on the other hand, Mn-sulfides are more soluble compared to Fe-sulfide minerals (Maynard, 2003); for instance, MnS has a pK_{sp} of 10.2 and FeS of 18.7 (Ball and Nordstrom, 1991). Thus, substituting Fe by Mn and Mg might stabilize vivianite in the presence of HS^- due to a lower reactivity of the incorporated cations towards HS^- than Fe. Our results suggest that substitution slightly enhanced dissolution rates due to changes in crystal size and roughness, as elemental loss indicative for minerals' dissolution was moderately larger for the Viv_sub treatments than for Viv treatments (Fig. 2, 4AB). However, variability among samples of the same treatment, likely due to strong spatial heterogeneity in the field (Fig. S19), makes it challenging to draw an unambiguous conclusion. Nevertheless, substitution significantly lowered the gain of solid-phase S (Fig. 5B, Table S17). In the Viv_sub treatments, the initial Fe content was lower (Table 2), resulting in a lower S binding capacity. A similar Fe to S ratio across all treatments at the high sulfide plot (Table S11) indicates that the Fe content controlled solid-phase S gain, which is further supported by a better retention capacity of Fe than Mn and Mg at the high sulfide plot. Overall, the incorporation of Mn and Mg appears to affect mineral reactivity and destabilizes the vivianite crystal structure at low and high sulfide conditions. This suggests that authigenic vivianite, in which Fe is frequently substituted by other cations, might be more reactive and less efficient in binding P under changing environmental conditions.

In addition, our data suggest that the presence of other cations changed transformation pathways. At low Eh, Mn geochemistry is controlled by carbonate minerals rather than sulfides (Maynard, 2003), which could explain some differences in transformation products. For instance, siderite formation was only detected in Viv_sub treatments at the low sulfide plot based on Fe K-edge EXAFS LCF analysis. The presence of siderite was surprising as chemical calculations indicated that the porewater was undersaturated with respect to siderite at both field plots (Table S7, S8). However, at the low sulfide plot, the porewater was oversaturated with respect to rhodochrosite, a manganese carbonate ($MnCO_3$). Siderite and rhodochrosite form frequently solid-solution series (Huebner, 1969; Postma, 1980). Thus, we hypothesize that the presence of Mn in the Viv_sub treatments triggered rhodochrosite formation. The formed rhodochrosite likely had a high Fe content, due to localized high Fe concentrations and was thus identified as siderite by Fe K-edge EXAFS. Furthermore, Mn and Mg are likely to be incorporated in the formed green rust phases (Refait et al., 2001; Wang et al., 2022). A strong correlation between Mn and P (Table S30, S31) and the identification of P associated with Mn-oxides by P K-edge XANES (Fig. 4CD) suggest further that the presence of other divalent cations was important for P retention. The importance of Mn-minerals (P-bearing rhodochrosite and hureaulite) as a P retention phase has also been shown in natural settings (Hermans et al., 2019). Thus, the presence of other divalent cations might result in the formation of minerals, which can (partially) retain the released phosphate upon vivianite dis-

solution, and further research could expand on the investigation on the role of Mn as a P retention phase in coastal sediments.

4.3. Effect of the presence of $CaCO_3$ on P retention and speciation

In natural systems, the presence of HS^- can result in a sink-switch of P associated with Fe minerals to P associated with Ca minerals during early diagenesis (Ruttenberg and Berner, 1993; Millero et al., 2001). Phosphorus associated with Ca can include P sorbed to $CaCO_3$ (aragonite, calcite, Millero et al., 2001; Sø et al., 2011) or apatite minerals such as carbonate fluorapatite or hydroxyapatite (Ruttenberg and Berner, 1993; Schenau et al., 2000; Kraal et al., 2017). Due to the link of P with Ca, we investigated the effect of the presence of $CaCO_3$ inside the mesh bags on the P release upon vivianite dissolution.

Overall, the presence of $CaCO_3$ slightly lowered P loss (Fig. 4AB). However, the variability among samples within the treatment was greater than differences between treatments. Therefore, further research is needed to unambiguously determine the effect of $CaCO_3$ on P loss. Nevertheless, our results may provide some indications, as discussed in the following.

LCF of the P K-edge XANES did not detect P associated with Ca-minerals (sorbed, crystalline, or amorphous). We determined a sorption capacity of 13.7 μmol P/g for the used $CaCO_3$ (data not shown, sorption conducted at pH 7.7 in pre-equilibrated seawater). This sorption capacity aligns with previous results (Kraal et al., 2017). However, with only 0.21 g of $CaCO_3$ added per mesh bag, P adsorbed to $CaCO_3$ would contribute a maximum of 1% to the total P pool, falling below the detection limit of P K-edge XANES (Gustafsson et al., 2020). To detect P associated with Ca-minerals by P K-edge XANES, the formation of amorphous or crystalline Ca-minerals with a lower Ca:P ratio than P sorbed to $CaCO_3$ would have been required. Given the slow formation kinetics of crystalline Ca-minerals such as apatite (Griffin and Jurinak, 1973; Schenau et al., 2000), the formation of amorphous or meta-stable crystalline Ca-P phases may be more likely in our system. Although the porewater was supersaturated with respect to various crystalline and amorphous Ca-P phases (Table S7 to S10), the nucleation and crystal growth of all these phases may be retarded due to the presence of inhibitory cations and anions such as Mg^{2+} and carbonate alkalinity (Cao and Harris, 2008). Thus, the absence of detectable Ca-P phases in our LCF fits suggests that if Ca-P phases formed their contribution was below the detection limit of P K-edge XANES (~10%, Eriksson et al., 2016; Gustafsson et al., 2020).

In contrast to the LCF fits, synchrotron-based uXRF maps showed a weak positive correlation between Ca and P (Pearson correlation coefficient, ~ 0.2, Table S29, S31), suggesting that some P may have been retained by the present $CaCO_3$ or newly formed Ca-P phases, possibly explaining the slightly lower P loss observed in mesh bags containing $CaCO_3$. Another potential explanation for the decrease in P loss could be a reduction in advective and diffusive flow rates resulting from the addition of $CaCO_3$. In natural sediments, measurements of soluble reactive phosphate in pore waters of $CaCO_3$-rich sediments are much lower than in sediments with low or no $CaCO_3$ (Morse et al., 1985; Millero et al., 2001), indicating the importance of $CaCO_3$ for phosphate retention. Under environmental settings, the ratio of vivianite to other sediment components such as clay minerals and $CaCO_3$ would be substantially lower than in our studied mesh bags, which were strongly enriched in vivianite. Adjusting the ratio of vivianite to sediment matrix could enhance P retention further, helping in a clearer determination of the effect of $CaCO_3$ on P loss upon vivianite dissolution. This aspect is worth further investigation.

4.4. Environmental implications

Our experimental setup allowed us to gain information on the transformation pathways of vivianite under two contrasting conditions: (i) low sulfide, suboxic to anoxic conditions and (ii) high sulfide, euxinic conditions. To our knowledge, our results are the first study assessing vivianite transformation in-situ. In contrast to previous findings based on laboratory experiments, we found that vivianite was not completely dissolved during the 56-day-long field experiment highlighting slower transformation kinetics. Nevertheless, a substantial proportion of vivianite dissolved (at least 10% to 32% based on total Fe loss), followed partially by the precipitation of secondary minerals.

Under low sulfide conditions, at which vivianite was thermodynamically unstable, vivianite dissolution resulted in the release of Fe, Mn, Mg, and P and the formation of green rust. A nearly unchanged molar ratio of (Fe+Mn+Mg)/P in the solid phase highlighted the importance of green rust as a phosphate sorbent, supporting the findings of Xiong et al. (2023). Our results are of importance as the formation and stability of green rust and vivianite likely impacted P cycling in ancient anoxic oceans, with important implications for Earth's biogeochemical evolution (Swanner et al., 2020; Alcott et al., 2022).

Our results concerning vivianite transformation at high sulfidic conditions might explain why vivianite and Fe-sulfide minerals co-exist in natural sediments as complete vivianite dissolution may be inhibited under natural conditions (Dijkstra et al., 2014; Hsu et al., 2014). Nevertheless, we show that sulfide-mediated vivianite dissolution increased phosphate availability, as indicated by elevated solid-phase P losses from the mesh bags and increased (Fe+Mn+Mg)/P molar ratios in the remaining solid phase. Furthermore, vivianite containing impurities (Viv_sub), representative of authigenic vivianite, dissolved substantially more than unsubstituted vivianite (Viv). This finding suggests that substitution influences mineral reactivity and thus needs to be considered when studying the reactivity and stability of vivianite as a permanent P burial sink in the environment.

Overall, our findings show that upon changes in environmental conditions, such as reducing to euxinic conditions, vivianite-containing sediment could become a source of bioavailable P. This is important when considering past, current and future coastal systems. For instance, great parts of the Wadden Sea and the Elbe estuary are classified as eutrophic (OSPAR, 2023). Vivianite is present in sediments within the oligohaline section of the Elbe estuary (König et al., 1988; Van Put et al., 1994). Anticipated alterations in river discharge patterns and sea level-induced increases in mean high tide levels are expected to shift salinity levels upstream in the Elbe estuary (von Storch and Claussen, 2012). This increase in salinity will result in enhanced sulfate availability in the estuary's upstream region, potentially leading to increased sulfide production by sulfate reduction. Our results suggest that this process could lead to the dissolution and transformation of vivianite present in the sediments. Similar environmental changes can also be expected in other coastal regions. For instance, vivianite has been found at 1 cm sediment depth in the Chesapeake Bay (Li et al., 2015), one of the most well-studied estuaries in the world. Strong summer stratification in the Chesapeake Bay results in bottom water hypoxia, which induces sulfate reaction and thus HS^- production (Testa and Kemp, 2012). In the future, sea level rise is expected to enhance this by increasing salinity and thus sulfate availability in the Chesapeake Bay (Hong and Shen, 2012). Thus, vivianite present in coastal sediments, such as those found in the Elbe estuary and the Chesapeake Bay, represents a legacy of sedimentary P that could be destabilized, potentially enhancing coastal eutrophication.

Similar processes may have affected phosphate bioavailability during past geological periods characterized by glacial-interglacial sea level changes (Filippelli et al., 2007; Sundby et al., 2022). For instance, in continental margin sediments, vivianite can be an important P sink below the sulfate-methane transition zone (Burns, 1997; März et al., 2018). However, the position of the SMTZ is not static; it migrates within the sediment on glacial timescales (Henkel et al., 2012; März et al., 2018). For instance, Sundby et al. (2022) proposed a shallowing of the SMTZ during glacial time periods due to the destabilization of methane hydrates. This movement implies that vivianite formed below the shallow SMTZ during glacial periods might be destabilized when

the SMTZ moves downward. Thus, the potential dissolution of vivianite as a source of bioavailable phosphate due to the movement of the SMTZ and, thus position of high sulfide concentrations should be considered when assessing internal processes altering nutrient variations on glacial timescales.

Finally, our results indicate that post-depositional dissolution of vivianite due to changes in biogeochemistry could alter vivianite content in sediments. This is important to consider when vivianite is used to obtain information on paleo-environmental conditions (Taldenkova et al., 2010; Vuillemin et al., 2013; Dijkstra et al., 2018). Additionally, we show that sulfide-mediated vivianite dissolution enhances P bioavailability, results which may impact our understanding of primary production and Earth's biogeochemical evolution (Derry, 2015; Hao et al., 2020; Alcott et al., 2022).

5. Conclusions

We presented the first in-situ study investigating the transformation of unsubstituted and Mn-Mg-substituted vivianite with and without $CaCO_3$ in an intertidal sediment with low and high dissolved sulfide concentration. We identified transformation products and assessed the effect of substitution on mineral dissolution and secondary mineral formation. In addition, we determined how the presence of $CaCO_3$ alters phosphate retention upon vivianite dissolution. Under the studied conditions, vivianite dissolution resulted in a release of Fe, Mn, Mg, and P. We hypothesize that a protective layer of secondary minerals may have inhibited complete dissolution. Green rust minerals were the major transformation products at the low sulfide plot, while mackinawite formation dominated at the high sulfide plot, indicating the dominance of oxidative transformation and sulfidation, respectively. Formed green rust likely retained some of the released phosphate, while the low affinity of mackinawite towards phosphate resulted in an enhanced P loss at the high sulfidic plot. Substituted vivianite dissolved faster, likely due to smaller crystal size and enhanced crystal roughness. The presence of $CaCO_3$ slightly enhanced P retention and indicates that the presence of $CaCO_3$ may positively impact P retention during vivianite dissolution, which deserves further investigation to draw unambiguous conclusions. Overall, our findings are of significance for understanding Earth's past biogeochemical evolution and assessing future nutrient fluxes.

CRediT authorship contribution statement

L. Joëlle Kubeneck: Conceptualization, Formal analysis, Investigation, Methodology, Validation, Visualization, Writing – original draft, Writing – review & editing. **Luiza Notini:** Investigation, Validation, Writing – review & editing, Formal analysis. **Katherine A. Rothwell:** Investigation, Validation, Writing – review & editing, Formal analysis. **Giulia Fantappiè:** Investigation, Methodology, Writing – review & editing. **Thomas Huthwelker:** Investigation, Writing – review & editing. **Laurel K. ThomasArrigo:** Methodology, Supervision, Validation, Writing – review & editing, Formal analysis, Conceptualization. **Ruben Kretzschmar:** Conceptualization, Funding acquisition, Methodology, Project administration, Resources, Supervision, Validation, Writing – review & editing.

Declaration of competing interest

The authors declare that they have no known competing financial interests or personal relationships that could have appeared to influence the work reported in this paper.

Data availability

Data is available through ETH Zurich at https://doi.org/10.3929/ethz-b-000635104.

Acknowledgements

We thank Katrin Schulz (ETH Zürich) for assistance during XAS data collection and Kurt Barmettler (ETH Zürich) for assisting with laboratory analyses. We thank the National Park Administration, Landesbetrieb für Küstenschutz, Nationalpark und Meeresschutz Schleswig-Holstein, Germany for granting permission to conduct field experiments in the German National Park Wadden Sea. We acknowledge the Paul Scherrer Institute, Villigen, Switzerland (Proposal no. 20211802, PHOENIX beamline XO7MB) and MAX IV (Proposal no. 20210752) for the provision of synchrotron radiation facilities and thank Stuart Ansell for his support during data collection. We thank the ID21 Phosphorus XANES Spectra Database of the European Synchrotron for the compilation of P K-edge XANES spectra. This work received funding from the European Research Council (ERC) under the European Union's Horizon 2020 research and innovation program (grant agreement no. 788009-IRMIDYN-ERC-2017-ADG).

Appendix A. Supplementary material

Supplementary material related to this article can be found online at https://doi.org/10.1016/j.gca.2024.01.020.

References

Alcott, L.J., Mills, B.J., Bekker, A., Poulton, S.W., 2022. Earth's great oxidation event facilitated by the rise of sedimentary phosphorus recycling. Nat. Geosci. 15, 210–215.
Allen, G.C., Hush, N.S., 1967. Intervalence-transfer absorption. Part 1. Qualitative evidence for intervalence-transfer absorption in inorganic systems in solution and in the solid state. Prog. Inorg. Chem. 8, 357–389.
Alvarez, M., Rueda, E.H., Sileo, E.E., 2006. Structural characterization and chemical reactivity of synthetic Mn-goethites and hematites. Chem. Geol. 231, 288–299.
Asmala, E., Carstensen, J., Conley, D.J., Slomp, C.P., Stadmark, J., Voss, M., 2017. Efficiency of the coastal filter: nitrogen and phosphorus removal in the Baltic Sea. Limnol. Oceanogr. 62, S222–S238.
Ball, J.W., Nordstrom, D.K., 1991. WATEQ4F–User's manual with revised thermodynamic data base and test cases for calculating speciation of major, trace and redox elements in natural waters. Open-file report.
Benali, O., Abdelmoula, M., Refait, P., Génin, J.M.R., 2001. Effect of orthophosphate on the oxidation products of Fe(II)-Fe(III) hydroxycarbonate: the transformation of green rust to ferrihydrite. Geochim. Cosmochim. Acta 65, 1715–1726.
Benning, L.G., Wilkin, R.T., Barnes, H., 2000. Reaction pathways in the Fe–S system below 100 °C. Chem. Geol. 167, 25–51.
Berner, R.A., 1981. A new geochemical classification of sedimentary environments. J. Sediment. Res. 51, 359–365.
Bocher, F., Géhin, A., Ruby, C., Ghanbaja, J., Abdelmoula, M., Génin, J.M.R., 2004. Coprecipitation of Fe(II-III)hydroxycarbonate green rust stabilised by phosphate adsorption. Solid State Sci. 6, 117–124.
Bouwman, A., Bierkens, M., Griffioen, J., Hefting, M., Middelburg, J., Middelkoop, H., Slomp, C., 2013. Nutrient dynamics, transfer and retention along the aquatic continuum from land to ocean: towards integration of ecological and biogeochemical models. Biogeosciences 10, 1–22.
Brady, M.P., Tostevin, R., Tosca, N.J., 2022. Marine phosphate availability and the chemical origins of life on Earth. Nat. Commun. 13, 5162.
Bronner, R., Thompson, K., Dreher, C., Runge, E., Voggenreiter, E., Shuster, J., Wan, B., Joshi, P., Fischer, S., Duda, J., et al., 2023. Co-reduction of Fe(III) and S^0 drives Fe-S biomineral formation and phosphate mobilisation. Geochem. Perspect. Lett. 24, 27–32.
Burns, S.J., 1997. Early diagenesis in Amazon fan sediments. Proc. Ocean Drill. Program Sci. Results 155, 531–538.
Cao, X., Harris, W., 2008. Carbonate and magnesium interactive effect on calcium phosphate precipitation. Environ. Sci. Technol. 42, 436–442.
Claff, S.R., Sullivan, L.A., Burton, E.D., Bush, R.T., 2010. A sequential extraction procedure for acid sulfate soils: partitioning of iron. Geoderma 155, 224–230.
Cline, J.D., 1969. Spectrophotometric determination of hydrogen sulfide in natural waters 1. Limnol. Oceanogr. 14, 454–458.
Conley, D.J., Paerl, H.W., Howarth, R.W., Boesch, D.F., Seitzinger, S.P., Havens, K.E., Lancelot, C., Likens, G.E., 2009. Controlling eutrophication: nitrogen and phosphorus.
Derry, L.A., 2015. Causes and consequences of mid-proterozoic anoxia. Geophys. Res. Lett. 42, 8538–8546.
Dijkstra, N., Hagens, M., Egger, M., Slomp, C.P., 2018. Post-depositional formation of vivianite-type minerals alters sediment phosphorus records. Biogeosciences 15, 861–883.
Dijkstra, N., Kraal, P., Kuypers, M.M., Schnetger, B., Slomp, C.P., 2014. Are iron-phosphate minerals a sink for phosphorus in anoxic Black Sea sediments? PLoS ONE 9, e101139.

Duverger, A., Berg, J.S., Busigny, V., Guyot, F., Bernard, S., Miot, J., 2020. Mechanisms of pyrite formation promoted by sulfate-reducing bacteria in pure culture. Front. Earth Sci. 8, 588310.
Egger, M., Jilbert, T., Behrends, T., Rivard, C., Slomp, C.P., 2015. Vivianite is a major sink for phosphorus in methanogenic coastal surface sediments. Geochim. Cosmochim. Acta 169, 217–235.
Ekstrom, E.B., Learman, D.R., Madden, A.S., Hansel, C.M., 2010. Contrasting effects of Al substitution on microbial reduction of Fe(III) (hydr)oxides. Geochim. Cosmochim. Acta 74, 7086–7099.
Eriksson, A.K., Hillier, S., Hesterberg, D., Klysubun, W., Ulén, B., Gustafsson, J.P., 2016. Evolution of phosphorus speciation with depth in an agricultural soil profile. Geoderma 280, 29–37.
Filippelli, G.M., Latimer, J.C., Murray, R.W., Flores, J.A., 2007. Productivity records from the Southern Ocean and the equatorial Pacific Ocean: testing the glacial shelf-nutrient hypothesis. Deep-Sea Res., Part 2, Top. Stud. Oceanogr. 54, 2443–2452.
Froelich, P.N., 1988. Kinetic control of dissolved phosphate in natural rivers and estuaries: a primer on the phosphate buffer mechanism 1. Limnol. Oceanogr. 33, 649–668.
Génin, J.M.R., Bourrié, G., Trolard, F., Abdelmoula, M., Jaffrezic, A., Refait, P., Maitre, V., Humbert, B., Herbillon, A., 1998. Thermodynamic equilibria in aqueous suspensions of synthetic and natural Fe(II)-Fe(III) green rusts: occurrences of the mineral in hydromorphic soils. Environ. Sci. Technol. 32, 1058–1068.
Griffin, R., Jurinak, J., 1973. The interaction of phosphate with calcite. Soil Sci. Soc. Am. J. 37, 847–850.
Grundl, T.J., Haderlein, S., Nurmi, J.T., Tratnyek, P.G., 2011. Introduction to aquatic redox chemistry. In: Aquatic Redox Chemistry. ACS Publications, pp. 1–14.
Gunnars, A., Blomqvist, S., Johansson, P., Andersson, C., 2002. Formation of Fe(III) oxyhydroxide colloids in freshwater and brackish seawater, with incorporation of phosphate and calcium. Geochim. Cosmochim. Acta 66, 745–758.
Gunnars, A., Blomqvist, S., Martinsson, C., 2004. Inorganic formation of apatite in brackish seawater from the Baltic Sea: an experimental approach. Mar. Chem. 91, 15–26.
Gustafsson, J.P., Braun, S., Tuyishime, J.M., Adediran, G.A., Warrinnier, R., Hesterberg, D., 2020. A probabilistic approach to phosphorus speciation of soils using P K-edge XANES spectroscopy with linear combination fitting. Soil Syst. 4, 26.
Hao, J., Knoll, A.H., Huang, F., Schieber, J., Hazen, R.M., Daniel, I., 2020. Cycling phosphorus on the Archean Earth: Part II. Phosphorus limitation on primary production in Archean ecosystems. Geochim. Cosmochim. Acta 280, 360–377.
Heinrich, L., Rothe, M., Braun, B., Hupfer, M., 2021. Transformation of redox-sensitive to redox-stable iron-bound phosphorus in anoxic lake sediments under laboratory conditions. Water Res. 189, 116609.
Henkel, S., Mogollón, J.M., Nöthen, K., Franke, C., Bogus, K., Robin, E., Bahr, A., Blumenberg, M., Pape, T., Seifert, R., et al., 2012. Diagenetic barium cycling in Black Sea sediments - a case study for anoxic marine environments. Geochim. Cosmochim. Acta 88, 88–105.
Hermans, M., Lenstra, W.K., van Helmond, N.A., Behrends, T., Egger, M., Séguret, M.J., Gustafsson, E., Gustafsson, B.G., Slomp, C.P., 2019. Impact of natural re-oxygenation on the sediment dynamics of manganese, iron and phosphorus in a euxinic Baltic Sea basin. Geochim. Cosmochim. Acta 246, 174–196.
Hong, B., Shen, J., 2012. Responses of estuarine salinity and transport processes to potential future sea-level rise in the Chesapeake Bay. Estuar. Coast. Shelf Sci. 104, 33–45.
Howes, B., Teal, J., 1994. Oxygen loss from Spartina alterniflora and its relationship to salt Marsh oxygen balance. Oecologia 97, 431–438.
Hsu, T.W., Jiang, W.T., Wang, Y., 2014. Authigenesis of vivianite as influenced by methane-induced sulfidization in cold-seep sediments off southwestern Taiwan. J. Asian Earth Sci. 89, 88–97.
Huebner, J.S., 1969. Stability relations of rhodochrosite in the system manganese-carbon-oxygen. Am. Mineral. 54, 457–481.
Jeong, H.Y., Han, Y.S., Park, S.W., Hayes, K.F., 2010. Aerobic oxidation of mackinawite (FeS) and its environmental implication for arsenic mobilization. Geochim. Cosmochim. Acta 74, 3182–3198.
Kester, D.R., Duedall, I.W., Connors, D.N., Pytkowicz, R.M., 1967. Preparation of artificial seawater. Limnol. Oceanogr. 12, 176–179.
König, I., Knauth, H.D., Koopmann, C., Wagner, F., Wagner, U., 1988. Mössbauer studies of sediments and suspended matter from the river Elbe. Hyperfine Interact. 41, 811–814.
Kraal, P., Dijkstra, N., Behrends, T., Slomp, C.P., 2017. Phosphorus burial in sediments of the sulfidic deep Black Sea: key roles for adsorption by calcium carbonate and apatite authigenesis. Geochim. Cosmochim. Acta 204, 140–158.
Krom, M.D., Berner, R.A., 1980. Adsorption of phosphate in anoxic marine sediments 1. Limnol. Oceanogr. 25, 797–806.
Krom, M.D., Berner, R.A., 1981. The diagenesis of phosphorus in a nearshore marine sediment. Geochim. Cosmochim. Acta 45, 207–216.
Kubeneck, L.J., Lenstra, W.K., Malkin, S.Y., Conley, D.J., Slomp, C.P., 2021. Phosphorus burial in vivianite-type minerals in methane-rich coastal sediments. Mar. Chem. 231, 103948.
Kubeneck, L.J., ThomasArrigo, L.K., Rothwell, K.A., Kaegi, R., Kretzschmar, R., 2023. Competitive incorporation of Mn and Mg in vivianite at varying salinity and effects on crystal structure and morphology. Geochim. Cosmochim. Acta 346, 231–244.
Kukkadapu, R.K., Zachara, J.M., Fredrickson, J.K., Kennedy, D.W., 2004. Biotransformation of two-line silica-ferrihydrite by a dissimilatory Fe (III)-reducing bacterium: formation of carbonate green rust in the presence of phosphate. Geochim. Cosmochim. Acta 68, 2799–2814.
Lenstra, W.K., Egger, M., Van Helmond, N.A., Kritzberg, E., Conley, D.J., Slomp, C.P., 2018. Large variations in iron input to an oligotrophic Baltic Sea estuary: impact on sedimentary phosphorus burial. Biogeosciences 15, 6979–6996.
Li, W., Joshi, S.R., Hou, G., Burdige, D.J., Sparks, D.L., Jaisi, D.P., 2015. Characterizing phosphorus speciation of Chesapeake Bay sediments using chemical extraction, ^{31}P NMR, and X-ray absorption fine structure spectroscopy. Environ. Sci. Technol. 49, 203–211.
Liu, H., Lu, X., Li, M., Zhang, L., Pan, C., Zhang, R., Li, J., Xiang, W., 2018. Structural incorporation of manganese into goethite and its enhancement of Pb(II) adsorption. Environ. Sci. Technol. 52, 4719–4727.
Mackey, J., Collins, R., 1967. The Mössbauer effect of iron in ion exchange resins. J. Inorg. Nucl. Chem. 29, 655–660.
Manceau, A., Nagy, K.L., 2012. Quantitative analysis of sulfur functional groups in natural organic matter by XANES spectroscopy. Geochim. Cosmochim. Acta 99, 206–223.
März, C., Riedinger, N., Sena, C., Kasten, S., 2018. Phosphorus dynamics around the sulphate-methane transition in continental margin sediments: authigenic apatite and Fe(II)phosphates. Mar. Geol. 404, 84–96.
Maynard, J.B., 2003. Manganiferous sediments, rocks, and ores. In: Treatise on Geochemistry 7, p. 407.
McCammon, C.A., Burns, R.G., 1980. The oxidation mechanism of vivianite as studied by Mössbauer spectroscopy. Am. Mineral. 65, 361–366.
Millero, F., Huang, F., Zhu, X., Liu, X., Zhang, J.Z., 2001. Adsorption and desorption of phosphate on calcite and aragonite in seawater. Aquat. Geochem. 7, 33–56.
Mori, H., Ito, T., 1950. The structure of vivianite and symplesite. Acta Crystallogr. 3, 1–6.
Morse, J.W., Zullig, J.J., Bernstein, L.D., Millero, F.J., Milne, P.J., Mucci, A., Choppin, G.R., 1985. Chemistry of calcium carbonate-rich shallow water sediments in the Bahamas. Am. J. Sci. 285, 147–185.
Murphy, T.P., Lawson, A., Kumagai, M., Nalewajko, C., 2001. Release of phosphorous from sediments in Lake Biwa. Limnol. 2, 119–128.
Notini, L., Schulz, K., Kubeneck, L.J., Grigg, A.R.C., Rothwell, K.A., Fantappiè, G., ThomasArrigo, L.K., Kretzschmar, R., 2023. A new approach for investigating iron mineral transformations in soils and sediments using ^{57}Fe-labeled minerals and ^{57}Fe Mössbauer spectroscopy. Environ. Sci. Technol. 57, 10008–10018.
Notini, L., ThomasArrigo, L.K., Kaegi, R., Kretzschmar, R., 2022. Coexisting goethite promotes Fe (II)-catalyzed transformation of ferrihydrite to goethite. Environ. Sci. Technol. 56, 12723–12733.
Nriagu, J.O., 1972. Stability of vivianite and ion-pair formation in the system $Fe_3(PO_4)_2$-H_3PO_4-H_2O. Geochim. Cosmochim. Acta 36, 459–470.
O'Connell, D.W., Jensen, M.M., Jakobsen, R., Thamdrup, B., Andersen, T.J., Kovacs, A., Hansen, H.C.B., 2015. Vivianite formation and its role in phosphorus retention in Lake Ørn. Denmark Chem. Geol. 409, 42–53.
OSPAR, 2023. Eutrophication thematic assessment. In: OSPAR: Quality Status Report 2003. OSPAR Commission, London.
Postma, D., 1980. Formation of siderite and vivianite and the pore-water composition of a recent bog sediment in Denmark. Chem. Geol. 31, 225–244.
Poulton, S.W., Canfield, D.E., 2005. Development of a sequential extraction procedure for iron: implications for iron partitioning in continentally derived particulates. Chem. Geol. 214, 209–221.
Poulton, S.W., Krom, M.D., Raiswell, R., 2004. A revised scheme for the reactivity of iron(oxyhydr)oxide minerals towards dissolved sulfide. Geochim. Cosmochim. Acta 68, 3703–3715.
Pyzik, A.J., Sommer, S.E., 1981. Sedimentary iron monosulfides: kinetics and mechanism of formation. Geochim. Cosmochim. Acta 45, 687–698.
Ravel, B., Newville, M., 2005. ATHENA, ARTEMIS, HEPHAESTUS: data analysis for X-ray absorption spectroscopy using IFEFFIT. J. Synchrotron Radiat. 12, 537–541.
Refait, P., Abdelmoula, M., Trolard, F., Génin, J.M., Ehrhardt, J., Bourrie, G., 2001. Mössbauer and XAS study of a green rust mineral; the partial substitution of Fe^{2+} by Mg^{2+}. Am. Mineral. 86, 731–739.
Refait, P., Drissi, S., Pytkiewicz, J., Génin, J.M., 1997. The anionic species competition in iron aqueous corrosion: role of various green rust compounds. Corros. Sci. 39, 1699–1710.
Refait, P., Reffass, M., Landoulsi, J., Sabot, R., Jeannin, M., 2007. Role of phosphate species during the formation and transformation of the Fe (II-III) hydroxycarbonate green rust. Colloids Surf. A, Physicochem. 299, 29–37.
Ressler, T., 1998. WinXAS: a program for X-ray absorption spectroscopy data analysis under MS-Windows. J. Synchrotron Radiat. 5, 118–122.
Rickard, D., 1969. The chemistry of iron sulphide formation at low temperatures. Stockh. Contrib. Geol. 20, 67–95.
Rickard, D., Luther, G.W., 2007. Chemistry of iron sulfides. Chem. Rev. 107, 514–562.
Rickard, D., Schoonen, M.A., Luther III, G., 1995. Chemistry of iron sulfides in sedimentary environments. In: Geochemical Transformations of Sedimentary Sulfur. In: ACS Publications, pp. 168–193.
Roldán, R., Barrón, V., Torrent, J., 2002. Experimental alteration of vivianite to lepidocrocite in a calcareous medium. Clay Miner. 37, 709–718.
Rouzies, D., Millet, J.M., 1993. Mössbauer study of synthetic oxidized vivianite at room temperature. Hyperfine Interact. 77, 19–28.
Ruttenberg, K.C., Berner, R.A., 1993. Authigenic apatite formation and burial in sediments from non-upwelling, continental margin environments. Geochim. Cosmochim. Acta 57, 991–1007.

Sahoo, G., Fujieda, S., Shinoda, K., Suzuki, S., 2011. Influence of phosphate species on green rust I transformation and local structure and morphology of γ-FeOOH. Corros. Sci. 53, 2446–2452.

Schenau, S., Slomp, C., De Lange, G., 2000. Phosphogenesis and active phosphorite formation in sediments from the Arabian Sea oxygen minimum zone. Mar. Geol. 169, 1–20.

Schippers, A., Jørgensen, B.B., 2001. Oxidation of pyrite and iron sulfide by manganese dioxide in marine sediments. Geochim. Cosmochim. Acta 65, 915–922.

Schwertmann, U., Fechter, H., 1994. The formation of green rust and its transformation to lepidocrocite. Clay Miner. 29, 87–92.

Sø, H.U., Postma, D., Jakobsen, R., Larsen, F., 2011. Sorption of phosphate onto calcite; results from batch experiments and surface complexation modeling. Geochim. Cosmochim. Acta 75, 2911–2923.

Solé, V.A., Papillon, E., Cotte, M., Walter, P., Susini, J., 2007. A multiplatform code for the analysis of energy-dispersive X-ray fluorescence spectra. Spectrochim. Acta, Part B, At. Spectrosc. 62, 63–68.

Son, S., Hyun, S.P., Charlet, L., Kwon, K.D., 2022. Thermodynamic stability reversal of iron sulfides at the nanoscale: insights into the iron sulfide formation in low-temperature aqueous solution. Geochim. Cosmochim. Acta 338, 220–228.

von Storch, H., Claussen, M., 2012. Klimabericht für die Metropolregion Hamburg. Springer-Verlag.

Striggow, B., 2017. Field measurement of oxidation-reduction potential (ORP). US Environmental Protection Agency; Science and Ecosystem Support Division, 2017–07.

Sundby, B., Anschutz, P., Lecroart, P., Mucci, A., 2022. Ideas and perspectives: sea-level change, anaerobic methane oxidation, and the glacial-interglacial phosphorus cycle. Biogeosciences 19, 1421–1434.

Swanner, E.D., Lambrecht, N., Wittkop, C., Harding, C., Katsev, S., Torgeson, J., Poulton, S.W., 2020. The biogeochemistry of ferruginous lakes and past ferruginous oceans. Earth-Sci. Rev. 211, 103430.

Taldenkova, E., Bauch, H.A., Gottschalk, J., Nikolaev, S., Rostovtseva, Y., Pogodina, I., Ovsepyan, Y., Kandiano, E., 2010. History of ice-rafting and water mass evolution at the northern Siberian continental margin (Laptev Sea) during Late Glacial and Holocene times. Quat. Sci. Rev. 29, 3919–3935.

Testa, J.M., Kemp, W.M., 2012. Hypoxia-induced shifts in nitrogen and phosphorus cycling in Chesapeake Bay. Limnol. Oceanogr. 57, 835–850.

Thiel, J., Byrne, J.M., Kappler, A., Schink, B., Pester, M., 2019. Pyrite formation from FeS and H_2S is mediated through microbial redox activity. Proc. Natl. Acad. Sci. 116, 6897–6902.

ThomasArrigo, L.K., Mikutta, C., Byrne, J., Kappler, A., Kretzschmar, R., 2017. Iron (II)-catalyzed iron atom exchange and mineralogical changes in iron-rich organic freshwater flocs: an iron isotope tracer study. Environ. Sci. Technol. 51, 6897–6907.

Torrent, J., Schwertmann, U., Barron, V., 1987. The reductive dissolution of synthetic goethite and hematite in dithionite. Clay Miner. 22, 329–337.

Van Put, A., Van Grieken, R., Wilken, R.D., Hudec, B., 1994. Geochemical characterization of suspended matter and sediment samples from the Elbe river by EPXMA. Water Res. 28, 643–655.

Vandenberghe, R.E., De Grave, E., 2012. Application of Mössbauer spectroscopy in Earth sciences. In: Mössbauer Spectroscopy: Tutorial Book. Springer, pp. 91–185.

Vuillemin, A., Ariztegui, D., De Coninck, A., Lücke, A., Mayr, C., Schubert, C.J., Team, P.S., 2013. Origin and significance of diagenetic concretions in sediments of Laguna Potrok Aike, southern Argentina. J. Paleolimnol. 50, 275–291.

Wan, M., Schröder, C., Peiffer, S., 2017. Fe (III): S (-II) concentration ratio controls the pathway and the kinetics of pyrite formation during sulfidation of ferric hydroxides. Geochim. Cosmochim. Acta 217, 334–348.

Wang, X., Li, X., Wang, L., Lanson, B., Zhu, M., Ying, C., Liang, X., Feng, X., 2022. Effects of Mn or Al incorporation on the structure, composition, and As(III) adsorption of oxidized green rust. Chem. Geol. 611, 121124.

Wilfert, P., Meerdink, J., Degaga, B., Temmink, H., Korving, L., Witkamp, G.J., Goubitz, K., van Loosdrecht, M., 2020. Sulfide induced phosphate release from iron phosphates and its potential for phosphate recovery. Water Res. 171, 115389.

Wu, Z., Zhang, T., Lanson, B., Yin, H., Cheng, D., Liu, P., He, F., 2023. Sulfidation of Ni-bearing goethites to pyrite: the effects of Ni and implications for its migration between iron phases. Geochim. Cosmochim. Acta 353, 158–170.

Xiong, Y., Guilbaud, R., Peacock, C.L., Krom, M.D., Poulton, S.W., 2023. Phosphorus controls on the formation of vivianite versus green rust under anoxic conditions. Geochim. Cosmochim. Acta 351, 139–151.